

1 **Process-based evaluation of ENSO simulation sensitivity to**
2 **horizontal resolution in the Chinese Academy of Sciences FGOALS-**
3 **f3 Climate System Model**

4
5 Meng-Er Song¹, Lin Chen¹, Yongqiang Yu², Bo An², Jiuwei Zhao¹, Hai Zhi¹

6
7 ¹ State Key Laboratory of Climate System Prediction and Risk Management/Key Laboratory of
8 Meteorological Disaster, Ministry of Education/Collaborative Innovation Center on Forecast and
9 Evaluation of Meteorological Disasters, Nanjing University of Information Science and Technology,
10 Nanjing 210044

11 ² State Key Laboratory of Earth System Numerical Modeling and Application, Institute of Atmospheric
12 Physics, Chinese Academy of Sciences, Beijing, China

13
14
15
16 *Correspondence to:* Lin Chen (chenlin@nuist.edu.cn)

19 **Abstract.** The El Niño-Southern Oscillation (ENSO) is the most prominent mode of interannual climate
20 variability; its simulation performance represents a critical benchmark for evaluating the fidelity of
21 coupled climate models. Increasing model resolution is an effective approach to improve the climate
22 model performance; however, the impact of refining horizontal resolution from the hundred-kilometer
23 scale to the tens-of-kilometer scale on ENSO simulation, as well as the underlying mechanisms, remains
24 unclear. This study provides a process-based evaluation of ENSO behavior in two versions of the Chinese
25 Academy of Sciences Flexible Global Ocean–Atmosphere–Land System Finite-Volume version 3
26 (FGOALS-f3) climate system model: a low-resolution configuration (~100 km; FGOALS-f3-L, hereafter
27 f3-L) and a high-resolution configuration (~25 km; FGOALS-f3-H, hereafter f3-H). Using a reproducible
28 diagnostic framework, we assess how horizontal resolution influences ENSO amplitude, oscillation
29 irregularity, key air–sea coupling processes, and high-frequency (HF) atmospheric variability. The low-
30 resolution version severely overestimates ENSO amplitude, whereas f3-H produces amplitude closer to
31 the observation. Process-based diagnostics show that this improvement arises from the more realistic
32 representation of thermocline and zonal advection feedback processes in f3-H, which arises from the
33 more realistic representation of the meridional structure of ENSO-related zonal wind stress anomalies
34 over equatorial Pacific in f3-H and can be traced back to its improved horizontal resolution. The ENSO
35 cycle in f3-L exhibits excessive regularity, featuring periodic warm-cold transitions; while f3-H
36 reproduces an irregular oscillation resembling the observation. The excessive regularity in f3-L is
37 attributed to its coarser resolution, which limits the simulation performance of tropical cyclones and
38 consequently weakens high-frequency westerly wind activity over the tropical Pacific. The weak
39 stochastic forcing in f3-L is insufficient to disrupt its overly intense ENSO cycle, yielding an overly
40 regular oscillation. By identifying the structural sources of ENSO biases across resolutions, this study
41 provides a reproducible and model-agnostic framework for diagnosing resolution effects on ENSO
42 performance in climate models and informs future development of the FGOALS-f3 model family.

43

44 **1 Introduction**

45 El Niño-Southern Oscillation (ENSO), as one of the most prominent interannual variabilities in the
46 Earth's climate system, exerts a profound influence on regional and global climate (McPhaden et al.,
47 2006; Cai et al., 2021). Therefore, the ability to accurately simulate ENSO phenomenon serves as a
48 fundamental benchmark for evaluating the fidelity of coupled climate models (Timmermann et al., 2018).
49 Despite significant progress in the development of climate models, large inter-model spread remains in
50 ENSO characteristics across Coupled Model Intercomparison Project (CMIP) generations (Zhang et al.,
51 2020; Planton et al., 2021). Common biases include inaccuracies in simulating ENSO amplitude (Planton
52 et al., 2021), period (Lu et al., 2018), seasonal phase locking (Liao et al., 2023; Yan and Sun, 2024),
53 spatial distribution (Jiang et al., 2021), and intensity asymmetry (Zhao and Sun, 2022), as well as an
54 overly regular ENSO oscillation (Chen et al., 2016a; Guilyardi et al., 2020). These deficiencies reflect
55 systematic structural biases within models, which directly limit the predictive skill of dynamical models
56 (Barnston et al., 2012) and hinder the reliability of climate projection regarding how ENSO may evolve
57 under future climate change (Jiang et al., 2020a). Therefore, it is imperative to improve the fidelity of
58 ENSO simulation in climate models.

59 Horizontal resolution has long been recognized as an important factor influencing model behavior
60 (Yu et al., 2024). Motivated by this, the latest CMIP6 launched a dedicated High-Resolution Model Inter-
61 comparison Project (HighResMIP) (Eyring et al., 2016) to systematically assess the benefits of increased
62 resolution on model simulations. Previous studies have shown that as model resolution increases,
63 simulation capabilities for both the climate mean state and variability exhibit improvements (Dawson et
64 al., 2013; Chang et al., 2020). For example, high-resolution models demonstrate superior performance
65 over low-resolution counterparts in simulating the Asian summer monsoon (He et al., 2025a), the impact
66 of Tibetan Plateau thermal forcing on Asian summer monsoon (He et al., 2025b), the precipitation in
67 southern China (Zi et al., 2024), the spatial distribution and frequency of tropical cyclones (Kreussler et
68 al., 2021; Li et al., 2021), air-sea turbulent flux (Small et al., 2019), heat transport by boundary currents
69 (Docquier et al., 2019), ocean mesoscale eddies (Hallberg, 2013), and Antarctic sea ice (Docquier et al.,
70 2019). This is partly because higher resolution allows models to explicitly resolve finer-scale physical
71 processes, reducing their dependence on parameterization schemes. Furthermore, high-resolution models
72 facilitate a more accurate simulation of topographically sensitive regions, therefore improving the

73 simulation of atmosphere-ocean processes related to complex terrain (Bacmeister et al., 2014; Hewitt et
74 al., 2016). Then a pertinent inquiry arises: does the ENSO simulation benefit from the increased
75 resolution?

76 Regarding the impact of increased horizontal resolution on ENSO characteristics, previous studies
77 found that when the atmospheric horizontal resolution in climate models was increased from 3.8° (T30)
78 or 2.8° (T42) to 1° (T106), significant improvements can be found in the simulated ENSO period
79 (Guilyardi et al., 2004; Navarra et al., 2008) and ENSO amplitude (Hua et al., 2018). However, the
80 aforementioned studies were primarily based on the comparisons from ~400 km (or 300 km) to 100 km
81 scales. In the latest climate models participated in the HighResMIP, model resolutions have advanced
82 substantially, with some achieving 25 km resolution in atmospheric component and 10 km in oceanic
83 component. This higher resolution enables a more realistic reproduction of climate variability, such as
84 tropical cyclones (TCs) (Li et al., 2021) and tropical instability waves (Li et al., 2023). Yet, a critical
85 question remains unresolved: when model resolution reaches ~25 km, a scale that can reasonably
86 simulate weather-scale systems like TCs, does ENSO simulation also improve further?

87 ENSO is fundamentally driven by a number of coupled ocean-atmosphere feedbacks (Li, 1997; Jin
88 et al., 2006; Chen et al., 2015b; Chen et al., 2016a); however, some analyses regarding ENSO simulations
89 are often result-oriented, focusing only on changes in statistical indices while lacking sufficient
90 diagnostic analysis of the key air-sea feedback processes that shape ENSO's properties. Therefore, it is
91 necessary to conduct a process-oriented evaluation when comparing the ENSO simulation between
92 different resolution versions.

93 It is worth noting that the observational evidences have suggested the significant influence of
94 atmospheric "noise" on the development and evolution of ENSO (Chen et al., 2015a; Fedorov et al.,
95 2015). Here the atmospheric "noise" primarily refers to high-frequency (HF) wind activities such as
96 westerly wind bursts (Harrison and Vecchi, 1997; Fedorov, 2002), including synoptic and intra-seasonal
97 scales. TC and Madden-Julian Oscillation (MJO; Madden and Julian, 1971; Madden and Julian, 1972)
98 have been recognized as key sources of HF wind activities in recent studies (Ying et al., 2019; Liang and
99 Fedorov, 2021). Considering the atmospheric components in HighResMIP models can reach a horizontal
100 resolution of 50 km or finer (which is sufficient to reasonably reproduce TC features) and that the
101 simulation performance for TC and MJO activities improves with increasing resolution (Davis, 2018;

102 Tang et al., 2022; Roberts et al., 2025), a further question arises: does the improved simulation of HF
103 activities like TCs and MJO in high-resolution models contribute to improved ENSO simulation?

104 Motivated by these open questions, this study will conduct a process-oriented evaluation of ENSO
105 simulation for a Chinese climate model, the Flexible Global Ocean–Atmosphere–Land System Finite-
106 Volume version 3 (FGOALS-f3) climate system model that was developed by the Institute of
107 Atmospheric Physics, Chinese Academy of Sciences (IAP-CAS). FGOALS-f3 participated in
108 HighResMIP with both a low-resolution (~100 km; FGOALS-f3-L, hereafter f3-L) and a high-resolution
109 version (~25 km; FGOALS-f3-H, hereafter f3-H) (An et al., 2022; Bao et al., 2020). The high-resolution
110 version (f3-H) has been shown to have superior simulation performances over the low-resolution
111 counterpart (f3-L) in representing mesoscale vortices (An et al., 2022), tropical instability waves (Li et
112 al., 2023), TCs (Li et al., 2021), East Asian summer monsoon precipitation (Zi et al., 2024), and the
113 climatological mean states (Yu et al., 2024). Therefore, this study employs the CAS-developed f3-H and
114 f3-L to reveal the impact of model resolution on ENSO simulation performance and the underlying air-
115 sea coupling processes.

116 This model evaluation study will provide insights into the resolution sensitivity of ENSO-related
117 processes in FGOALS-f3 and establishes a diagnostic framework that can be applied to other coupled
118 models participating in CMIP6 and future CMIP phases. The remainder of this paper is organized as
119 follows. Section 2 describes the model configurations, observational datasets, and diagnostic framework.
120 Section 3 presents an overview of the ENSO characteristics in two versions of FGOALS-f3 model.
121 Section 4 and Section 5 demonstrate how the model horizontal resolution impacts the ENSO simulation.
122 Section 6 summarizes the findings and discusses implications for model development and evaluation.

123 **2. Model configurations, datasets, and diagnostic framework**

124 **2.1 Model configurations**

125 FGOALS-f3 is a fully coupled climate system model developed by State Key Laboratory of
126 Numerical Modeling for Atmospheric Sciences and Geophysical Fluid Dynamics (LASG), IAP-CAS,
127 which couples four component models using the CPL7 coupler (Craig et al., 2012). The four component
128 models are the atmospheric model FAMIL2.2 (He et al., 2019; Li et al., 2021), the ocean model
129 LICOM3.0 (Li et al., 2020), the land model CLM4.0 (Lawrence et al., 2011), and the sea ice model

130 CICE4.0 (Hunke and Lipscomb, 2010).

131 The atmospheric component FAMIL2.2 is the last version of the Finite-volume Atmospheric Model
132 developed by the LASG-IAP (FAMIL) (Li et al., 2021). FAMIL2.2 utilizes a finite-volume dynamical
133 core constructed on a cubed sphere grid that is globally partitioned into six tiles (Zhou et al., 2015). In
134 the vertical direction, the model uses hybrid coordinates over 32 layers, and the model top is 1 hPa. While
135 the horizontal resolution ranges from C96 (about 100 km) to C384 (about 25 km) across the different
136 resolution version. The oceanic component LICOM 3.0 is the third version of LASG-IAP Climate System
137 Ocean Model (LICOM) (Yu et al., 2018). LICOM 3.0 updated a new advection scheme and employed a
138 tripolar grid based on orthogonal curvilinear coordinates. The horizontal resolution of LICOM 3.0 can
139 vary flexibly between 1° and $1/20^\circ$. Sub-grid parametrization schemes employed in LICOM 3.0 include
140 the tidal mixing scheme, a buoyancy frequency related thickness diffusivity scheme, a vertical viscosity
141 and diffusion scheme, and a chlorophyll-a dependent solar penetration scheme, etc. A comprehensive
142 description of the physical package in LICOM3.0 can be found in Li et al. (2020). The land component
143 in FGOALS-f3 model is Community Land Model (CLM) version 4.0. This advanced model simulates
144 the water and momentum balances at the land surface and incorporates interactive carbon and nitrogen
145 cycles, allowing for a more realistic representation of vegetation dynamics and ecosystem processes
146 (Lawrence et al., 2011). In FGOALS-f3 model, sea ice is simulated using the Los Alamos Sea Ice Model
147 version 4.0 (CICE 4.0). This is a dynamic-thermodynamic model that simulates the evolution of sea ice
148 thickness, concentration, and velocity. It features multiple ice thickness categories and an elastic-viscous-
149 plastic (EVP) rheology to model ice deformation and dynamics (Hunke and Lipscomb, 2010).

150 The FGOALS-f3 model includes two versions: f3-L and f3-H (He et al., 2019; An et al., 2022). Both
151 models are participating in HighResMIP of CMIP6 and have successfully completed the Tier-1 and Tier-
152 3 experiments. These two models have the same components and physical processes. The sole distinction
153 between f3-H and f3-L lies in their horizontal resolution and the corresponding time steps within their
154 finite-volume cubed-sphere dynamical core (FV3). To maintain the stability of the integration for the
155 dynamical core, the two parameters (k_split and n_split) in FV3 are set to 6 and 15 in f3-H, respectively
156 (they are 2 and 6, respectively, in f3-L). The specific resolutions of each component of f3-L and f3-H
157 models are shown in Table 1.

158

159 **Table 1.** Resolution comparison of each component model between the FGOALS-f3-L model and the FGOALS-f3-
 160 H model

	FGOALS-f3-L	FGOALS-f3-H
Atmosphere	FAMIL2.2 (1°×1°, 32 levels)	FAMIL2.2 (0.25°×0.25°, 32 levels)
Ocean	LICOM3.0 (1°×1°, 30 levels)	LICOM3.0 (0.1°×0.1°, 55 levels)
Land	CLM4.0 (1.25°×0.9°)	CLM4.0 (0.31°×0.23°)
Sea Ice	CICE4.0 (1°×1°)	CICE4.0 (0.1°×0.1°)

161 The model data used in this study are obtained from the historical experiment outputs of f3-L and
 162 f3-H model. Considering the experiment outputs of f3-H (highresSST-present) start from 1950, the period
 163 during 1950-2014 for the two models are analyzed. The main variables used in this study include monthly
 164 sea surface temperature (SST), three-dimensional ocean currents (uo, vo, wo), oceanic potential
 165 temperature (thetao), surface wind stress (tauu, tauv), and net radiation flux (rsds, rsus, rlds, rlus, hfss,
 166 hfls); daily surface wind (uas, vas), precipitation (pr), six-hourly sea level pressure (SLP), 850 hPa wind
 167 (ua, va), 300 hPa and 500 hPa temperature (ta). All data is detrended before analyzing.

168 2.2 Observation and reanalysis datasets

169 The observational and reanalysis data used in this study include: 1) the monthly SST data obtained
 170 from the Hadley Centre Sea Ice and Sea Surface Temperature version 1.1 dataset (HadISST v1,1), with
 171 a horizontal resolution of 1°×1° (Rayner et al., 2003); 2) the monthly, daily, and hourly 10m wind fields
 172 are from the European Centre for Medium-Range Weather Forecasts (ECMWF) reanalysis data Fifth
 173 Generation (ERA5), with a horizontal resolution of 0.25°× 0.25° (Hersbach et al., 2020); 3) the daily
 174 precipitation is from the Global Precipitation Climate Program version 1.3 (GPCP v1.3), with a
 175 horizontal resolution of 2.5°× 2.5° (Adler et al., 2003); 4) the monthly sea surface wind stress data are
 176 provided by the ECMWF Ocean Reanalysis Data (ORAS5), with a horizontal resolution of 1°× 1° (Zuo
 177 et al., 2019) and America Ocean Data Assimilation Data Set version 2.2.4 (SODA v2.2.4), with a
 178 horizontal resolution of 0.5°× 0.5° (Carton and Giese, 2008); 5) the historical TC data are from the China
 179 Meteorological Administration (CMA) tropical cyclone best track dataset (Ying et al., 2014; Lu et al.,
 180 2021).

181 **2.3 Diagnostic framework**

182 This study employs a reproducible, model-agnostic diagnostic framework for evaluating resolution-
183 dependent ENSO behavior. Diagnostics include ENSO amplitude and spectrum, ENSO irregularity index,
184 Bjerknes index diagnosis and the corresponding total derivative decomposition, meridional distribution
185 index of zonal wind stress anomaly, oceanic zonal current decomposition, the HF atmospheric westerly
186 (easterly) wind index and the corresponding noise-to-signal ratio, and TC detection and metrics.

187 Throughout this study, an overbar $\overline{(\)}$ denotes the climatological mean field, and a prime $(\)'$
188 denotes the interannual anomaly obtained by removing the climatological seasonal cycle. The subscript
189 $'HF'$ indicates a HF (sub-90-day) filtered field. For example, u'_{HF} denotes the HF component of daily
190 zonal wind anomaly, obtained by applying a 90-day high-pass filter to the daily anomaly field. All
191 symbols are used consistently throughout the paper unless otherwise specified.

192 **2.3.1 ENSO amplitude, spectral analysis and ENSO irregularity index (CVT)**

193 Monthly SSTA is computed after removing the climatological seasonal cycle. ENSO amplitude is
194 measured by the standard deviation of Niño3.4 index (monthly SSTA averaged in 5°S–5°N, 170°–
195 120°W). Power spectra are derived using the multi-taper method following Thomson (1982). To
196 quantitatively evaluate the regularity of ENSO oscillation, we propose an ENSO irregularity index
197 based on the coefficient of variation of inter-event time intervals (CVT). This metric is computed
198 through the following steps.

199 First, ENSO events are identified using the 3-month running mean of the Niño3.4 index. A
200 warm (cold) event is defined when the 3-month running mean Niño3.4 index exceeds 0.5 (falls
201 below -0.5) standard deviation of the Niño3.4 index, and the event is considered to terminate when
202 the Niño3.4 index returns to within the ± 0.5 standard deviation range for at least two consecutive
203 months.

204 Second, the time interval between two successive events of the same sign is defined as the time
205 separation between adjacent event peaks (i.e., the month of maximum warming for warm events or
206 maximum cooling for cold events).

207 Third, the CVT is computed as the ratio of the standard deviation to the mean of these inter-
208 event intervals:

209
$$CVT = \frac{\sigma_T}{\mu_T} \quad (1),$$

210 where T denotes the set of all inter-event intervals, and μ_T and σ_T denote the mean and the
 211 standard deviation of these intervals, respectively.

212 Finally, the CVT is calculate separately for warm events (CVT_{warm}) and cold events (CVT_{cold}),
 213 and their average is taken as the final ENSO irregularity index used in this study. A larger CVT
 214 indicates more irregular ENSO oscillation with highly variable inter-event spacing, whereas a
 215 smaller CVT (approaching zero) indicates a more periodic and regular oscillation.

216 2.3.2 Bjerknes index diagnosis

217 In order to quantitatively analyze the air-sea coupling processes responsible for ENSO amplitude in
 218 FGOALS-f3 models, the diagnostic framework of BJ index (Kim and Jin, 2011a, 2011b) is performed in
 219 this study. The specific formulation is listed as follows:

220
$$BJ = \frac{R-\varepsilon}{2} \quad (2),$$

221
$$R = - \left(a_1 \frac{\langle \Delta \bar{u} \rangle_E}{L_x} + a_2 \frac{\langle \Delta \bar{v} \rangle_E}{L_y} \right) - \alpha_s + \mu_a \beta_u \langle -\frac{\partial \bar{T}}{\partial x} \rangle_E + \mu_a \beta_w \langle -\frac{\partial \bar{T}}{\partial z} \rangle_E + \mu_a \beta_h a_h \langle \frac{\bar{w}}{H_1} \rangle_E \quad (3),$$

222
$$\frac{\partial \langle h' \rangle_w}{\partial t} = -\varepsilon \langle h' \rangle_w - F[\tau_x'] \quad (4),$$

223
$$\langle Q' \rangle_E = -\alpha_s \langle T' \rangle_E \quad (5),$$

224
$$\langle H(\bar{w})T_{sub}' \rangle_E = a_h \langle T' \rangle_E \quad (6),$$

225
$$\langle h' \rangle_E - \langle h' \rangle_w = \beta_h [\tau_x'] \quad (7),$$

226
$$\langle H(\bar{w})w' \rangle_E = \beta_w [\tau_x'] \quad (8),$$

227
$$\langle u' \rangle_E = \beta_u [\tau_x'] + \beta_{uh} \langle h' \rangle_w \quad (9),$$

228
$$[\tau_x'] = \mu_a \langle T' \rangle_E \quad (10),$$

229 where u , v , and w are the three dimensional oceanic current velocity; T denotes sea surface temperature
 230 ($^{\circ}\text{C}$); $\langle \rangle_E$ and $\langle \rangle_w$ represent averaged volume of the eastern box region (5°S – 5°N , 170° – 90°W) and
 231 western box region (5°S – 5°N , 130°E – 170°W), respectively, from the ocean surface to the mixed layer
 232 depth; L_x and L_y denote the longitudinal and latitudinal lengths of the eastern box, respectively; H_1
 233 denotes the mixed layer depth (two complementary strategies for specifying H_1 are adopted in this study
 234 and their results are compared in Section 4.1). The coefficients a_1 and a_2 are obtained through linear
 235 regression using SST anomalies (SSTA) zonally or meridionally averaged at the boundaries and area-

236 averaged SSTA over the box. the " Δ " in equation (2) represents the differences of ocean current between
 237 the eastern and western boundaries. $H(\bar{W}) = \begin{cases} 1, \bar{W} > 0 \\ 0, \bar{W} \leq 0 \end{cases}$ is the step function to make sure only upward
 238 vertical motion is taken into account. Here, the Equation (1) defines the BJ index, serving as the primary
 239 metric for the growth rate examined in this analysis. The corresponding dynamic and thermodynamic
 240 feedbacks are expressed in Equation (2). In equation (3), the first term on the right-hand side is the
 241 damping process at the rate of ε ; the second term represents the Sverdrup transport across the equatorial
 242 Pacific basin. In Equations (4) to (9), α_s (s^{-1}) indicates the response of the thermodynamic damping to
 243 SSTA; μ_a ($N\ m^{-2}\ K^{-1}$) represents the response of surface wind stress anomalies (τ_x') to SSTA; β_u ($m\ s^{-1}$
 244 $(N\ m^{-2})^{-1}$) represents the response of upper ocean current anomalies (u_o') to τ_x' ; β_h ($m\ (N\ m^{-2})^{-1}$)
 245 indicates the response of the anomalous zonal slope of the equatorial Pacific thermocline to τ_x' ; β_w (m
 246 $s^{-1}\ (N\ m^{-2})^{-1}$) denotes the response of ocean upwelling anomalies (w_o') to τ_x' ; a_h ($K\ m^{-1}$) shows the
 247 effect of thermocline depth change on subsurface temperature anomalies.

248 Based on the above equations, the main contributing terms of the BJ index include two negative
 249 feedback processes: the dynamic damping by mean advection (MA; $-\left(a_1 \frac{\langle \Delta \bar{u} \rangle_E}{L_x} + a_2 \frac{\langle \Delta \bar{v} \rangle_E}{L_y}\right)$), the
 250 thermodynamic feedback (TD; $-\alpha_s$), and three positive feedback processes: the zonal advection
 251 feedback (ZA; $\mu_a \beta_u \langle -\frac{\partial \bar{T}}{\partial x} \rangle_E$), the thermocline feedback (TH; $\mu_a \beta_h a_h \langle \frac{\bar{w}}{H_1} \rangle_E$), and the Ekman feedback
 252 (EK; $\mu_a \beta_w \langle -\frac{\partial \bar{T}}{\partial z} \rangle_E$).

253 2.3.3 Meridional distribution index

254 To further quantify the meridional structure of ENSO-related τ_x' , a meridional distribution index
 255 (MDI) that was proposed by Chen et al. (2015b), is employed. The MDI is defined as:

$$256 \quad MDI = \frac{\int_{-10^\circ}^{10^\circ} \tau_x'(y) |y| dy}{\int_{-10^\circ}^{10^\circ} \tau_x'(y) dy} \quad (11),$$

257 where y denotes latitude, and $\tau_x'(y)$ represents the meridional profile of the normalized τ_x' . The
 258 normalized τ_x' obtained by regressing the zonal wind stress anomaly field onto the Niño4 region (5°S–
 259 5°N, 160°E–150°W) averaged zonal wind stress anomalies and then averaged over the Niño4 longitude
 260 range (160°E–150°W). The MDI provides a quantitative measure of the meridional concentration of
 261 ENSO-related τ_x' within the equatorial band. Specifically, a smaller MDI indicates that τ_x' is more
 262 concentrated near the equator, whereas a larger MDI indicates a broader meridional distribution.

263 2.3.4 Oceanic zonal current decomposition

264 ENSO-related zonal current anomaly (u'_o) in the equatorial region is composed of anomalous
 265 zonal geostrophic currents (u'_g) and anomalous Ekman currents (u'_e) (Su et al., 2010; Su et al., 2014).
 266 The specific formulas of u'_g and u'_e are listed below:

$$267 \quad u'_g = -\frac{g\partial^2 D'}{\beta\partial y^2} \quad (12),$$

$$268 \quad u'_e = \frac{1}{\rho H_1} \frac{r_s \tau'_x + \beta y \tau'_y}{r_s^2 + (\beta y)^2} \quad (13),$$

269 where β and r_s are the planetary vorticity gradient and Rayleigh dissipation rate (0.5 day^{-1}),
 270 respectively; τ'_y denotes the sea meridional wind stress anomaly; H_1 denotes the mean mixed layer
 271 depth, and ρ is the seawater density.

272 2.3.5 HF westerly (easterly) wind index and noise-to-signal ratio

273 An index regarding the HF zonal wind anomalies is used to quantitatively measure the intensity of
 274 HF westerly (easterly) wind activity in the f3-L and f3-H models. This index (named WWI index and
 275 EWI index) is defined as the integration of the averaged zonal HF westerly (easterly) wind over a fixed
 276 region (5°S – 5°N , 120°E – 180°). The formula is as follows:

$$277 \quad WWI \text{ index} = \int_{time1}^{time2} u_{HF}' dt, \quad u_{HF}' > 1m/s \quad (14),$$

$$278 \quad EWI \text{ index} = \int_{time1}^{ti} u_{HF}' dt, \quad u_{HF}' < -1m/s \quad (15),$$

279 where u_{HF}' represents the daily zonal wind anomaly after applying a 90-day high-pass filter, *time1* and
 280 *time2* represent the start and end time of the integrated period, respectively. In this study, the development
 281 period of ENSO event (January to August) is selected as the integrated period.

282 A noise-to-signal ratio (*NSR*) metric is proposed to quantify the relative magnitude of stochastic
 283 atmospheric forcing compared to the ENSO signal. The *NSR* is defined as:

$$284 \quad NSR = \frac{\sigma(u'_{HF})}{\sigma(SSTA_{Ni\tilde{n}o3.4})} \quad (16),$$

285 where $\sigma(u'_{HF})$ is the standard deviation of 90-day high-pass-filtered zonal wind anomalies averaged over
 286 the western equatorial Pacific (5°S – 5°N , 120°E – 180°), and $\sigma(SSTA_{Ni\tilde{n}o3.4})$ denotes the standard deviation
 287 of Niño3.4 index. A larger *NSR* indicates stronger stochastic forcing relative to the ENSO signal, and
 288 vice versa.

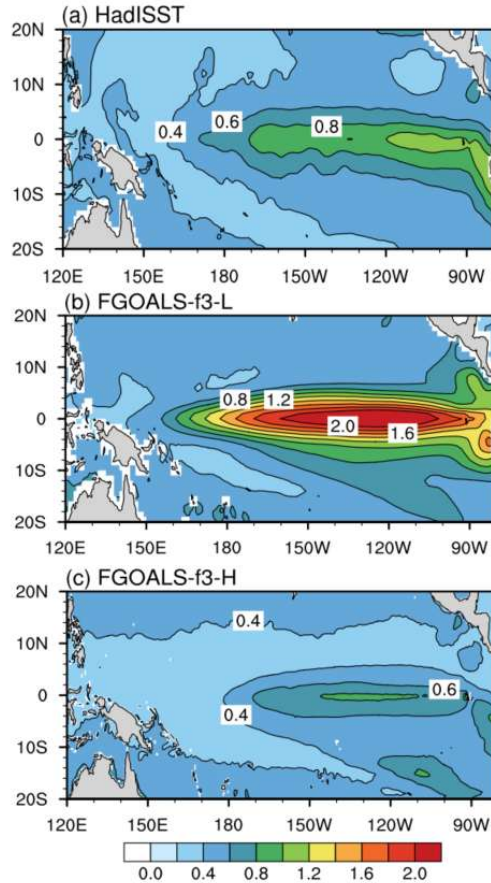
289 2.3.6 TC detection and metrics

290 The TC detection algorithm developed by the Geophysical Fluid Dynamics Laboratory
291 (<https://www.gfdl.noaa.gov/tstorms/>; Zhao et al., 2023) was used to detect TC activities in FGOALS-f3
292 model. The basic identification criteria and steps are: 1) a local minimum SLP is found within a maximum
293 distance of 3,000 km; 2) the wind speed at 850 hPa for this vortex exceed 17 m/s; 3) the absolute value
294 of the vorticity is greater than $1.5 \times 10^{-4} \text{ s}^{-1}$; 4) The temperature within 1200 km of the vortex center is
295 higher than that in the 1200-2400 km radius at 300-500 hPa, indicating a warm core structure; 5) The
296 lifespan of this TC should be at least three days (72h).

297 We further employ two metrics, i.e, accumulated cyclone energy (ACE) and TC track density
298 (TCTD), to assess the TC activity in FGOALS-f3 models. The ACE index (Bell et al., 2000) in each grid
299 cell is defined as the sum of the squares of the maximum surface wind speeds for all TCs occurring within
300 a $4^\circ \times 4^\circ$ grid cell over all 6-hourly periods (i.e., $ACE = \sum_i V_{max}^2$, where i denotes the i th TC in a grid cell
301 and V_{max} denotes its maximum surface wind speed). The TCTD in each grid is defined as the sum of the
302 number of TCs that have passed through the region within a distance of $4^\circ \times 4^\circ$ from the grid center.

303 3. Evaluation of ENSO Characteristics in f3-L and f3-H

304 Figure 1 shows the spatial distribution of the standard deviation (STD) of SSTA over the tropical
305 Pacific. In both the high- and low-resolution versions of FGOALS-f3, the interannual variability of SSTA
306 is concentrated in the central-eastern equatorial Pacific (Fig. 1b-c), which is spatially consistent with the
307 observation (Fig. 1a). However, significant differences exist in the ENSO amplitude. Specifically, the
308 STD of the Niño3.4 index is 0.79°C in the observation, 1.53°C in f3-L, and 0.62°C in f3-H, respectively.
309 This indicates that f3-L severely overestimates the ENSO amplitude, whereas f3-H's simulation is much
310 closer to the observation. Considering that the ENSO amplitude simulated in f3-L is approximately 2.5
311 times that of f3-H, this study will firstly address the causes of the stronger ENSO amplitude in f3-L
312 compared to its counterpart in f3-H.

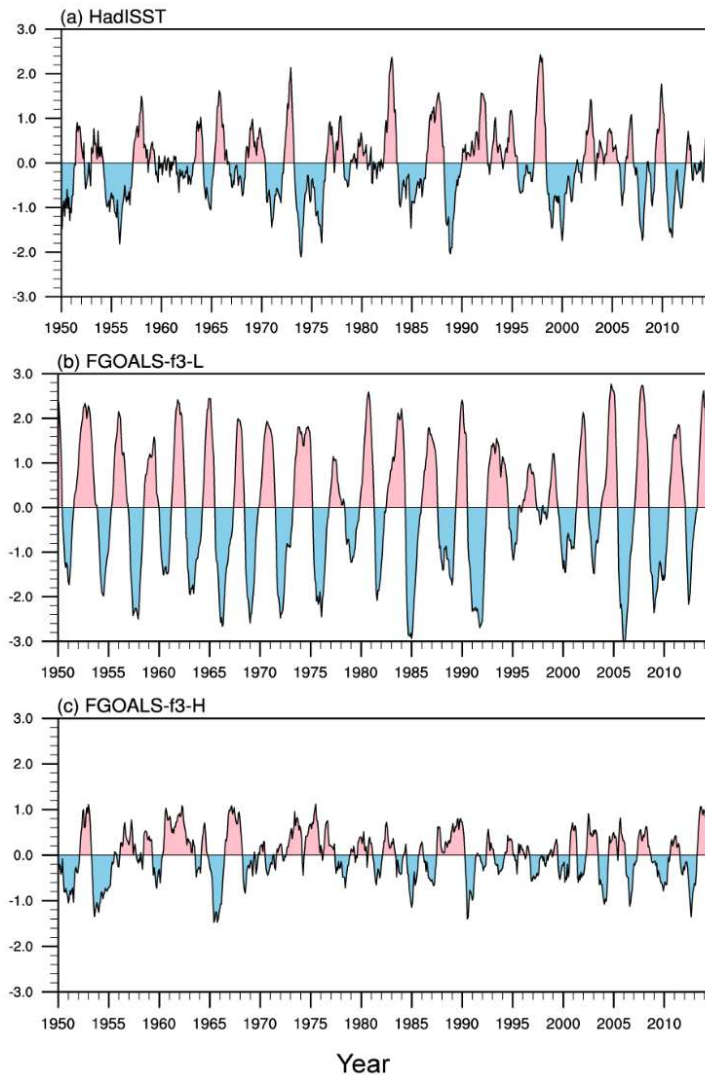


313
314
315

Figure 1. The standard deviation of SSTA (shading, units: °C) for (a) Observation (HadISST), (b) f3-L and (c) f3-H.

316
317
318
319
320
321
322
323
324
325

Figure 2 presents the time series of the Niño3.4 index for the observation and the two model versions. Obviously, the oscillation intensity of Niño3.4 index in f3-L is much stronger than that in the observation and f3-H, consistent with the results of the STD analysis (Fig. 1). Another notable difference lies in the regularity of the oscillation: ENSO events in f3-L exhibit highly periodic behavior, with a regular transition between warm and cold phases. In contrast, the ENSO evolution in both the observation and f3-H exhibit obvious irregularity. Furthermore, we conduct the power spectrum analysis on the Niño3.4 indices (Fig. 3). In the observation, the power spectrum is characterized by a broad band of 2–8 years. However, the power spectrum in f3-L shows a sharp and significant unimodal peak at approximately 3-year period, with excessive concentration of ENSO energy at this dominant period. In contrast, f3-H reproduces a broadband spectral distribution similar to the observation.



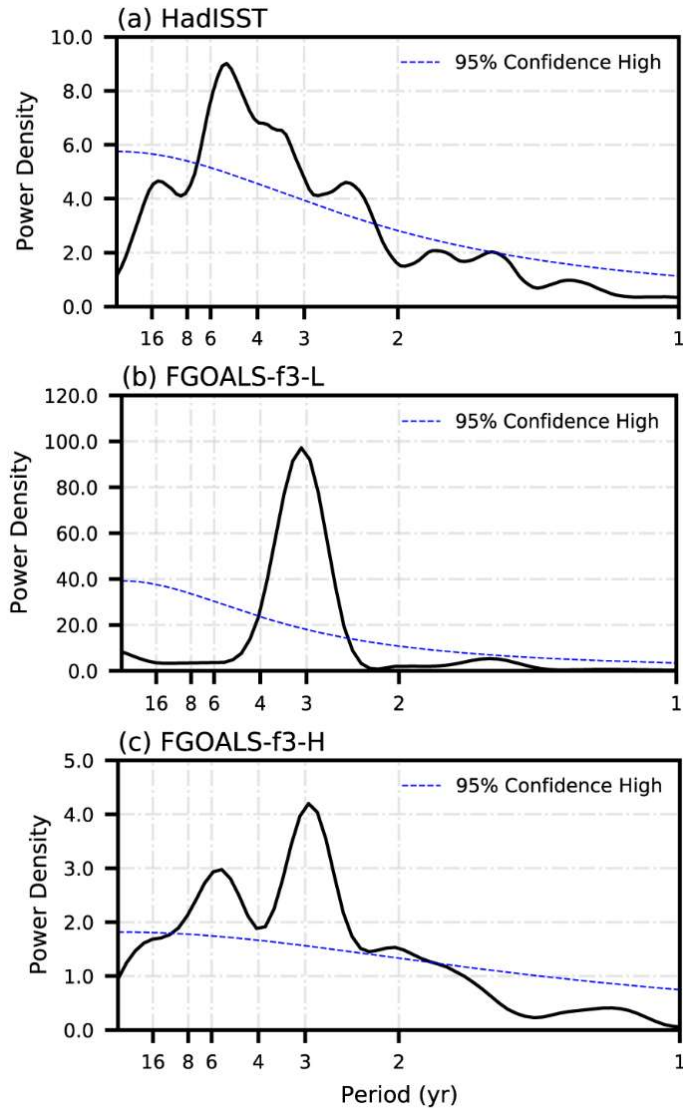
326
 327 **Figure 2.** Temporal evolution of Niño3.4 index (the averaged SSTA in the Pacific Niño3.4 region (5°S–5°N, 170°W–
 328 120°W), units: °C) for (a) Observation (HadISST), (b) f3-L and (c) f3-H.

329 Based on the proposed ENSO irregularity index, we calculated the *CVT* for the observation, f3-L
 330 and f3-H. As shown in Table 2, the *CVT* values are 0.61, 0.17, and 0.53 for the observation, f3-L and f3-
 331 H, respectively. The results clearly indicate that ENSO oscillation in f3-L is excessively regular compared
 332 to the observation (*CVT* of 0.17 vs. 0.61), whereas f3-H produces a degree of irregularity much closes to
 333 the observation. Therefore, the second question this study will address is: what causes the overly regular
 334 oscillation in f3-L, while f3-H captures more realistic irregularity?

335 Table 2. The ENSO irregularity index (*CVT*) for the observation, f3-L and f3-H.

	Observation	f3-L	f3-H
<i>CVT</i>	0.61	0.17	0.53

336



337
 338 **Figure 3.** The power spectra of Niño3.4 index for (a) Observation (HadISST), (b) f3-L and (c) f3-H. The blue line
 339 in the plots is the 95% confidence level.

340 **4. Process-based Diagnosis of ENSO Amplitude Differences**

341 **4.1 Diagnostic analysis based on the BJ index**

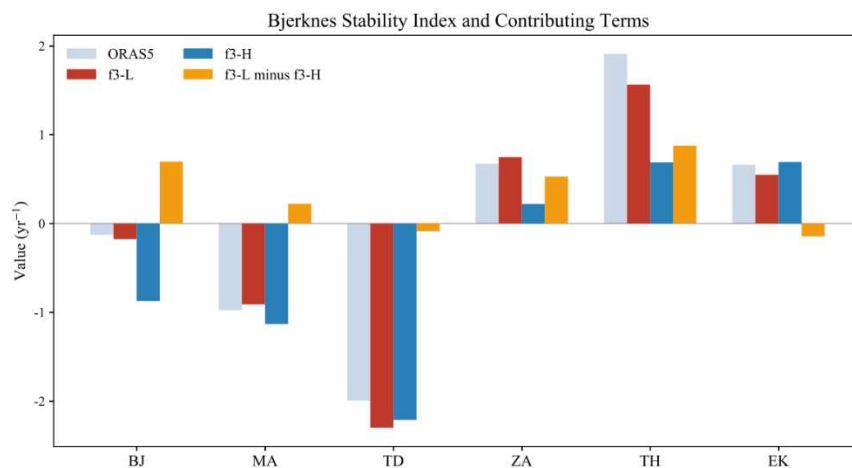
342 To investigate the physical mechanisms responsible for the ENSO amplitude difference between the
 343 high- and low-resolution versions, we apply the BJ index framework to quantitatively diagnose the
 344 stability of the coupled ocean-atmosphere system in both models. When applying the BJ index or the
 345 commonly used mixed-layer heat budget diagnosis, one practical issue is the choice of mixed layer depth
 346 (MLD) and whether the results are sensitive to this choice. We therefore first examine the spatial
 347 distribution of the climatological MLD in f3-L and f3-H. Here the MLD is defined as the depth at which
 348 the ocean temperature is 0.8°C lower than the SST, following Wang et al. (2012) and Chen et al. (2016b).
 349 As shown in Figure S1, the climatological MLD exhibits a pronounced zonal variation along the
 350 equatorial Pacific: it is relatively shallow in the far eastern Pacific and gradually deepens toward the

351 central equatorial Pacific. Moreover, the MLD differs between the two model versions, with the eastern
 352 box-mean values of approximately 65 m in f3-L and 50 m in f3-H over the eastern equatorial Pacific (i.e.,
 353 the eastern box used in the BJ index calculation). Given this zonal and inter-model variability, we adopt
 354 two complementary MLD strategies in the BJ index diagnostic.

355 **Strategy 1 (Constant MLD):** A fixed MLD of a constant value is applied to both f3-L and f3-H
 356 when computing the BJ index. This approach follows the conventional practice in previous BJ index
 357 studies (e.g., Kim and Jin, 2011a, 2011b; Chen et al., 2019a, 2019b) and facilitates a direct comparison
 358 between the two simulations under an identical diagnostic framework. From the perspective of the BJ-
 359 index eastern-box average, the climatological mean MLD over the eastern equatorial Pacific is
 360 approximately 65 m in f3-L and 50 m in f3-H. Therefore, in this first approach, we use a constant value
 361 of 65 m for both simulations.

362 The BJ index results under Strategy 1 are shown in Figure 4. Figure 4 presents the BJ index
 363 calculated using a fixed MLD of 65 m for the reanalysis, f3-L and f3-H, as well as their difference (f3-L
 364 minus f3-H). The results demonstrate that, although both models yield negative BJ indices, the value for
 365 f3-L is significantly larger (i.e., less negative) than that for f3-H. According to the physical interpretation
 366 of the BJ index (Jin et al., 2006; Kim and Jin, 2011a; 2011b), the less negative BJ index in f3-L indicates
 367 that the coupled air-sea system in f3-L is more unstable than that in f3-H. This more unstable coupled
 368 system is more favorable for ENSO growth, thereby leading to a stronger ENSO amplitude in f3-L than
 369 that in f3-H.

370



371

372 **Figure 4.** BJ index and the corresponding main contributing terms for the reanalysis (ORAS5; grey bars), f3-L (red
 373 bars), f3-H (blue bars) and their difference (f3-L minus f3-H, orange bars). Here the BJ index is calculated using a
 374 fixed MLD of 65 m. The five contributing terms include dynamic damping by mean advection (MA), thermodynamic
 375 damping feedback (TD), zonal advection feedback (ZA), thermocline feedback (TH) and Ekman feedback (EK).

376 It is worth noting that the BJ index derived from the reanalysis is not more negative than that of f3-

377 L, despite the observed ENSO amplitude being slightly weaker than that simulated by f3-L. This
378 inconsistency can be attributed to two factors. First, reanalysis products carry inherent uncertainties, and
379 direct comparison between reanalysis-derived and model-derived BJ indices should be interpreted with
380 caution. Second, the BJ index is a linear diagnostic framework that does not account for nonlinear
381 processes, including nonlinear atmospheric responses, semi-stochastic atmospheric noise (i.e., the HF
382 zonal wind anomalies discussed in this study), and oceanic nonlinear processes such as nonlinear
383 dynamical heating (Wei et al., 2026). In other words, while the BJ index is a useful tool for assessing
384 whether the linear air–sea coupling framework favors ENSO growth, the actual ENSO amplitude is
385 jointly determined by linear coupling, nonlinear processes, and stochastic forcing. This represents an
386 inherent limitation of the BJ index framework. Therefore, a comprehensive evaluation of ENSO
387 simulation requires not only the BJ index analysis of linear feedback processes but also diagnostics
388 beyond the linear framework to assess the roles of nonlinear processes and stochastic forcing, as
389 addressed in Section 5 of this study. In the following, our primary focus is on examining the differences
390 in the BJ index and its contributing terms between f3-L and f3-H.

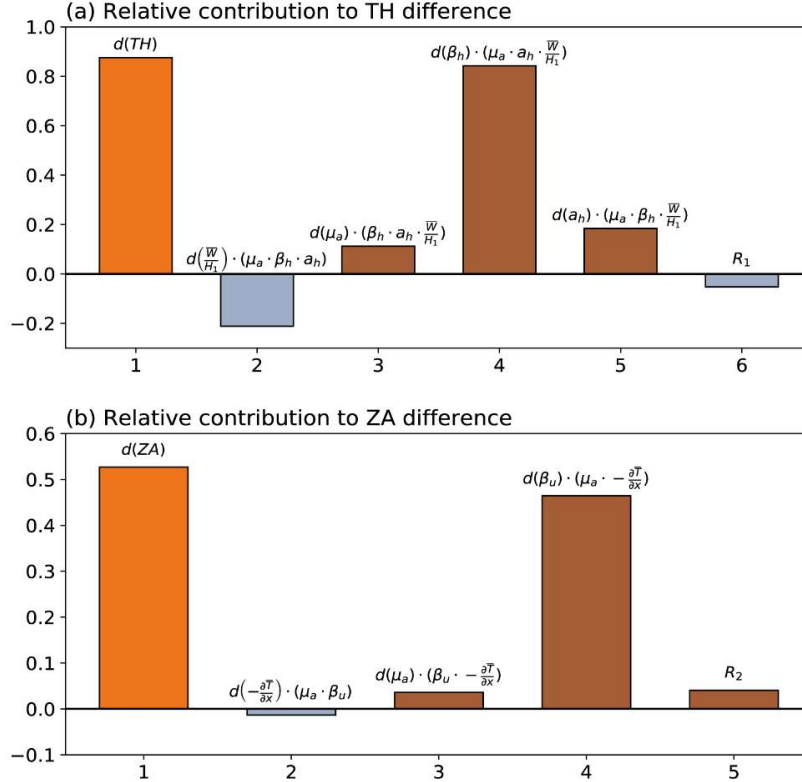
391 A further question arises: which physical processes contribute to the more unstable coupled system
392 in f3-L? By examining the differences in the five contributing terms of the BJ index (orange bars in Fig.
393 4), we find that the differences in the thermocline feedback (TH) term and the zonal advection feedback
394 (ZA) term are the dominant contributors to the BJ index difference (i.e., the system stability) between
395 the two model versions. Therefore, the subsequent analysis will focus on the physical mechanisms
396 responsible for the stronger TH and ZA terms in f3-L relative to f3-H.

397 **Strategy 2 (Longitude-varying MLD):** Each model version uses its own longitude-dependent
398 climatological MLD (averaged over the equatorial band, 5°S–5°N) when computing the BJ index. This
399 approach accounts for zonal variations and inter-model differences in stratification, providing a more
400 physically realistic diagnostic. In this approach, when calculating the BJ index, we diagnose the mixed-
401 layer temperature anomaly above the longitudinally varying climatological MLD (Figure S1) within the
402 three-dimensional eastern equatorial Pacific box.

403 Figure S2 presents the BJ index and its contributing terms calculated using the longitude-varying
404 MLD for the reanalysis, f3-L, and f3-H, as well as their difference (f3-L minus f3-H). The main results
405 are broadly consistent with those obtained under Strategy 1. Specifically, the BJ index of f3-H remains
406 more negative than that of f3-L, which largely explains the weaker ENSO amplitude in f3-H; and the BJ
407 index difference between the two models is still primarily attributable to the TH and ZA terms. The only

408 notable discrepancy between the two strategies lies in the MA term, which represents the dynamic
409 damping by mean zonal and meridional advection. In brief, under the longitude-varying MLD strategy,
410 the shallower MLD in f3-H means that the vertical averaging is taken over a thinner layer, in which the
411 poleward (damping) branch dominates more strongly, resulting in a more negative MA term in f3-H
412 compared to f3-L. A detailed analysis regarding the MA difference between f3-H and f3-L is provided in
413 the supplementary material. Overall, the sensitivity test demonstrates that the core conclusions of the BJ
414 index analysis, namely, the more unstable coupled system in f3-L and the dominant roles of the TH and
415 ZA terms are robust across both MLD strategies.

416 According to the definition of the BJ index (see Eq. (3)), each ocean dynamic term consists of two
417 components: one related to the mean state and the other to air-sea feedback processes. Considering that
418 both components may contribute to the differences in the TH and ZA terms between f3-L and f3-H, we
419 calculate the relative contributions of each component to the total difference using a total derivative
420 decomposition. As shown in Figure 5a, the stronger TH term in f3-L compared to f3-H (bar 1) primarily
421 arises from the difference in β_h (bar 4). The differences in μ_a and a_h make minor contributions, while
422 the mean state differences and the covariance term make negative contributions. Thus, the dominant
423 factor responsible for the stronger TH term in f3-L is the difference in β_h . Similarly, for the stronger ZA
424 term in f3-L, the results (Fig. 5b) show that the difference in ZA term (bar 1) is primarily determined by
425 the difference in β_u (bar 4), while the difference in a_h and the covariance term have marginal
426 contributions.



427

428

429

430

431

432

433

434

435

436

Figure 5. (a) Contributions of different components to the change in TH term. Bar 1 indicates the change in TH term [f3-L minus f3-H, $d(TH)$]. Bar 2 denotes the contribution from the mean state part change [$d(\bar{w}/H_1)$] to the change in TH term. Bar 3, 4 and 5 indicate the contributions from the air-sea feedbacks [$d(\mu_a)$, $d(\beta_h)$ and $d(a_h)$] to the change in TH term, respectively. Bar 6 is the residual, which denotes the contribution from the covariant changes of both the mean state part and the air-sea feedbacks. (b) same as (a) but for the zonal advection feedback (ZA). Bar 1 indicate the change in ZA term [f3-L minus f3-H, $d(ZA)$]. Bar 2 denotes the contribution from the mean state part change [$d(\partial \bar{T} / \partial x)$] to the change in ZA term. Bar 3 and Bar 4 indicate the contributions from the air-sea feedbacks [$d(\mu_a)$ and $d(\beta_u)$], respectively. Bar 5 is the residual, representing the contribution from the covariant changes of both the mean state part and the air-sea feedbacks.

437

4.2 Resolution dependence of the β_h feedback process difference

438

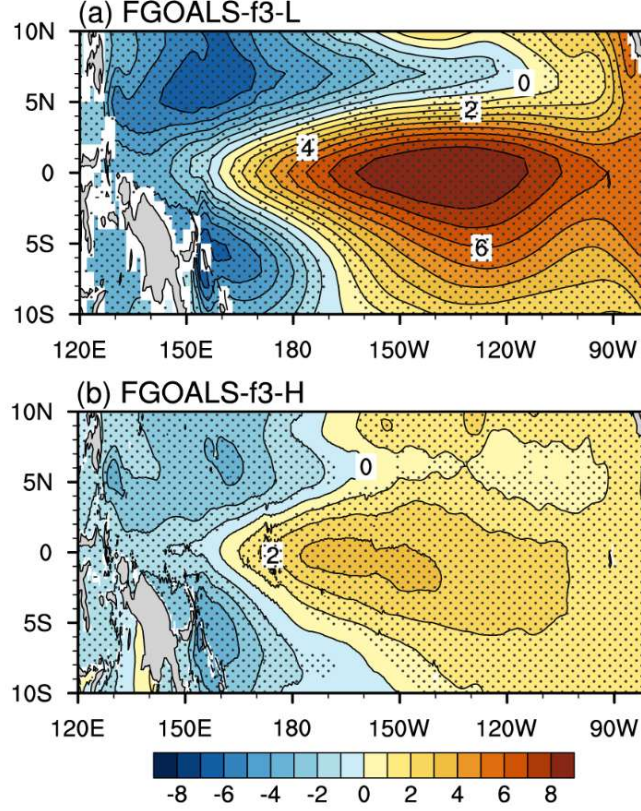
439

440

441

442

The air-sea feedback process β_h represents the response of the equatorial Pacific thermocline tilt to τ_x' . Figure 6 shows the regression of thermocline depth anomalies onto zonal wind stress anomalies for the two models. Both models reproduce the expected pattern: in response to positive τ_x' over the equatorial Pacific, the anomalous thermocline depth (D') deepens in the eastern equatorial Pacific and shoals in the western equatorial Pacific. However, the response is much stronger in f3-L than in f3-H.



443
 444 **Figure 6.** Distribution of the response of thermocline depth anomaly to zonal wind stress anomaly [β_h ; units: $\text{m} (\text{N m}^{-2})^{-1}$] for (a) f3-L and (b) f3-H. Based on the linear relationship between sea surface height anomaly (SSHA) and
 445 thermocline depth anomaly (D'), the SSHA is used as a proxy of D' . The D' response to zonal wind stress anomaly
 446 is derived through regressing the SSHA field onto the averaged zonal wind stress anomaly over equatorial Pacific
 447 (5°S – 5°N , 120°E – 100°W). The stippling in this plot denotes the regression coefficient exceeding a confidence level
 448 of 99% by using Student's t test.
 449

450 Based on the Sverdrup balance relationship (Jin, 1997; Li, 1997), the response of the D' to τ_x' is
 451 primarily determined by the mean equatorial thermocline depth (\bar{H}) and τ_x' :

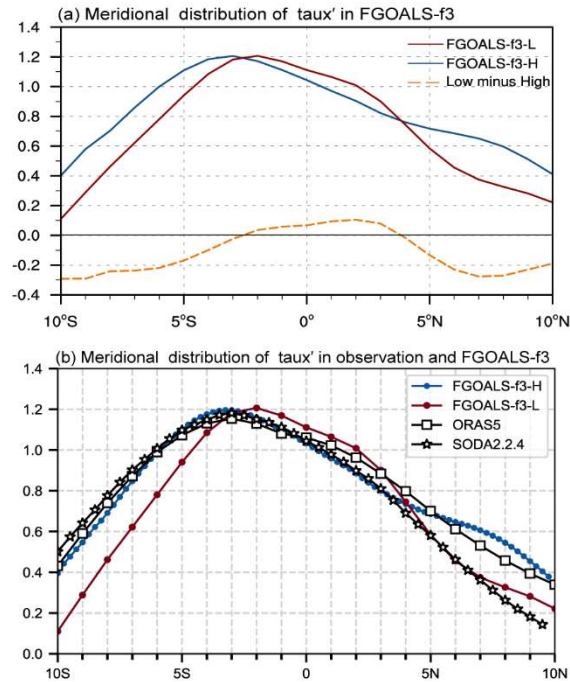
$$452 \quad \frac{\partial D'}{\partial x} = \frac{\tau_x'}{\rho g \bar{H}} \quad (17),$$

453 where ρ is the seawater density and g is the reduced gravity. We first examine the mean thermocline
 454 depth in both models and find that the difference in \bar{H} between f3-L and f3-H is negligible (figure not
 455 shown). Therefore, the difference in \bar{H} is not the primary cause.

456 Previous studies (Chen et al., 2015b; Chen et al., 2019a) have pointed out that the meridional
 457 structure of τ_x' is another key factor influencing the strength of β_h . Figure 7a presents the meridional
 458 structure of τ_x' for the two models and their difference (orange, f3-L minus f3-H). A significant
 459 difference exists: although the regression results show the same magnitude of τ_x' within the equatorial
 460 Pacific (5°S – 5°N), the τ_x' in f3-L is meridionally more concentrated near the equator (0°) than that in

461 f3-H. Since the τ_x' closer to equator is more effective in influencing D' (Chen et al., 2015b; Chen et al.,
 462 2019a), this more equatorially-confined meridional structure of τ_x' in f3-L inevitably results in a
 463 stronger response of D' to τ_x' (i.e., a larger β_h).

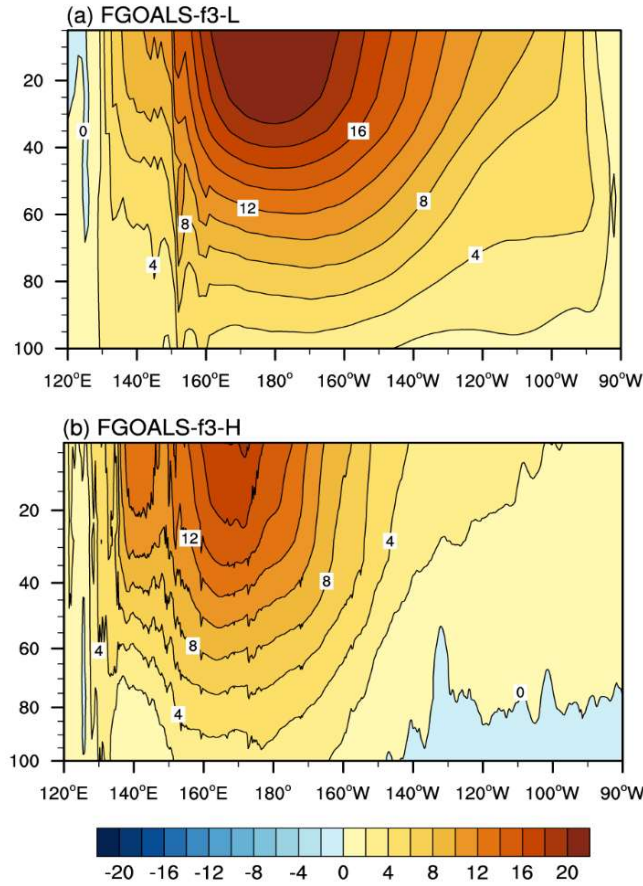
464 Furthermore, we compare the meridional structure of ENSO-related τ_x' in the two model versions
 465 with two reanalysis datasets. As shown in Fig. 7b, the meridional structures of τ_x' in the two reanalysis
 466 products (black lines) are very similar between 10°S–5°N, while some discrepancies exist within 5°N–
 467 10°N region. For the models, the f3-H (25 km atmospheric resolution) shows a τ_x' meridional structure
 468 in the equatorial region (5°S–5°N) that substantially resembles both reanalysis datasets. In contrast, the
 469 meridional structure of τ_x' within 5°S–5°N in f3-L (100 km atmospheric resolution) shows obvious
 470 discrepancies from the two reanalysis datasets. This suggests that model horizontal resolution can
 471 influence ENSO simulation by affecting the meridional distribution of τ_x' . The higher horizontal
 472 resolution is conducive to the more realistic representation of equatorial τ_x' meridional structure,
 473 thereby yielding a more reasonable thermocline feedback and ENSO amplitude.



474
 475 **Figure 7.** Meridional structure of normalized zonal wind stress anomalies [units: $\text{N m}^{-2} (\text{N m}^{-2})^{-1}$] averaged over the
 476 Niño4 longitude range (160°E–150°W) for (a) the result of f3-L (red solid line), f3-H (blue solid line) and their
 477 difference (orange dash line, f3-L minus f3-H). In this plot, all the data are both interpolated onto a $1^\circ \times 1^\circ$ grid to
 478 facilitate the comparison; (b) the results of ORAS5 (black line marked by square, with a $1^\circ \times 1^\circ$ grid), SODA2,2,4
 479 (black line marked by asterisk, with a $0.25^\circ \times 0.25^\circ$ grid), f3-L (red line marked by circle, with a $1^\circ \times 1^\circ$ grid) and
 480 f3-H (blue line marked by circle, with a $0.25^\circ \times 0.25^\circ$ grid). The normalized zonal wind stress anomalies are obtained
 481 by regressing the zonal wind stress anomalies field onto the Niño4 region (5°S–5°N, 160°E–150°W) averaged zonal
 482 wind stress anomalies.

483 **4.3 Resolution dependence of the β_u feedback process**

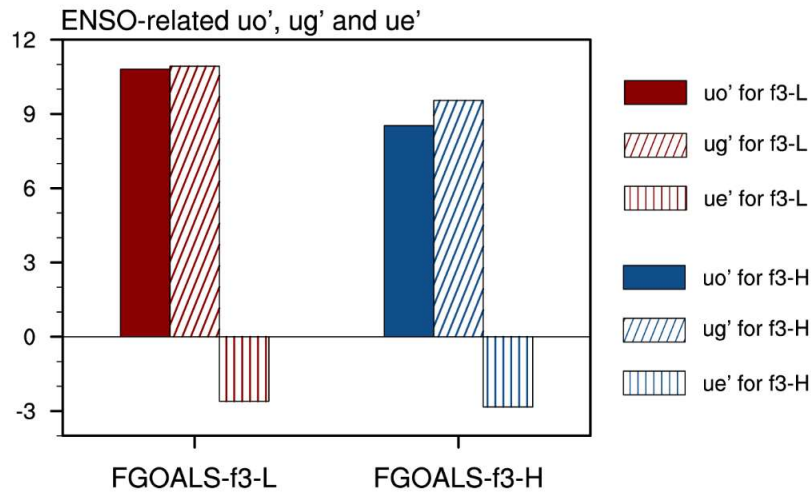
484 The air-sea feedback process β_u represents the response of the equatorial Pacific upper ocean zonal
 485 current anomaly (u'_o) to τ'_x . Figure 8 shows the equatorial profile for the response of u'_o to τ'_x in both
 486 models. Both models simulate eastward u'_o a unit eastward τ'_x in equatorial Pacific, but the response
 487 is significantly stronger in f3-L than in f3-H.



488 **Figure 8.** Vertical profile (averaged over 5°S–5°N) of the response of zonal ocean current anomaly (u'_o) to the zonal
 489 wind stress anomaly [β_u ; units: $\text{m s}^{-1} (\text{N m}^{-2})^{-1}$] for (a) f3-L and (b) f3-H. The u'_o response to zonal wind stress
 490 anomaly is derived through regressing the u'_o field onto the averaged zonal wind stress anomaly over equatorial
 491 Pacific (5°S–5°N, 120°E–100°W).
 492

493 Considering that ENSO-related u'_o in the equatorial region is composed of anomalous zonal
 494 geostrophic currents (u'_g) and anomalous Ekman currents (u'_e) (see Section 2.3.4), we first diagnose the
 495 response of u'_g and u'_e to wind stress anomalies (Fig. 9). In both versions, the response of u'_o to τ'_x
 496 is primarily contributed by the response of u'_g to τ'_x , while the contribution of u'_e is much smaller.
 497 This indicates that the difference in u'_g response to τ'_x is the main cause of the difference in β_u
 498 between the two model versions. Based on the geostrophic formula (Eq. (12)), the magnitude of u'_g is
 499 related to the second-order meridional derivative of D' . Since the meridional structure of D' (Figure 6)

500 exhibits a parabolic shape (peaking at equator and decreasing poleward), a stronger D' in the equatorial
 501 region corresponds to a larger value of second-order meridional derivative ($-\frac{\partial^2 D'}{\partial y^2}$) and, consequently, a
 502 stronger u'_g . As the D' response to τ'_x is primarily modulated by the $\beta_{\bar{h}}$ process, the difference in the β_u
 503 between the f3-L and f3-H is also primarily attributed to difference in the $\beta_{\bar{h}}$ process. That is, the
 504 stronger $\beta_{\bar{h}}$ in f3-L leads to a stronger D' , which in turn induces a stronger u'_g and u'_o and ultimately
 505 resulting in a stronger β_u .

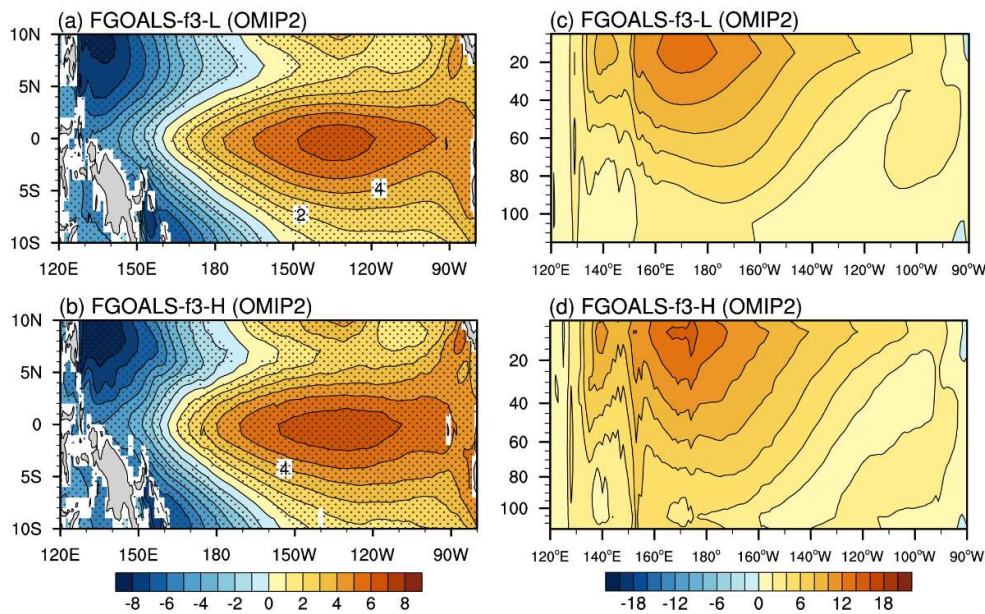


506 **Figure 9.** The ENSO-related zonal current anomalies (u') averaged over 0–65m, zonal geostrophic current anomalies
 507 (u'_g) and zonal Ekman current anomalies (u'_e) along the equatorial eastern Pacific (2°S–2°N, 180°–80°W) for f3-L
 508 (red bar) and f3-H (blue bar). The ENSO-related zonal current anomalies, zonal geostrophic current anomalies and
 509 zonal Ekman current anomalies are obtained by regressing it anomalies field onto the zonal wind stress anomalies
 510 averaged over Niño4 region (5°S–5°N, 160°E–150°W), respectively.
 511

512 4.4 Comparison with OMIP simulations

513 It should be noted that although our conclusions drawn from Coupled General Circulation Model
 514 (CGCM) indicate that the improved ENSO simulation is closely linked to the increased atmospheric
 515 resolution, the potential influence of oceanic horizontal resolution on ENSO simulation also merits brief
 516 examination. For instance, from the perspective of the oceanic component of CGCM (OGCM), Li et al.
 517 (2025) examined the oceanic zonal current and thermocline depth anomalies to zonal wind forcing by
 518 analyzing the outputs from Ocean Model Intercomparison Project 2 (OMIP2, Griffies et al. 2016) and
 519 found that the oceanic response to wind forcing is a key factor influencing ENSO simulation. Therefore,
 520 the resolution-induced contrast between the OMIP experiment and the CMIP experiment (i.e., the
 521 “historical” experiment) is a noteworthy phenomenon that warrants explanation.

522 According to the CMIP6’s protocol, OMIP2 experiments are forced by the identical atmospheric
 523 reanalysis datasets, thus providing an ideal framework to isolate biases originating from the oceanic
 524 component. Both f3-L and f3-H have participated in OMIP2, with respective oceanic horizontal
 525 resolutions of approximately 1° and 0.1°. To further assess the potential impact of oceanic horizontal
 526 resolution on ENSO simulation, we compare the key air-sea feedback terms (β_h and β_u) between f3-L
 527 and f3-H OMIP2 outputs. As shown in figure 10, the response of zonal current and thermocline depth
 528 anomalies to the identical τ_x' are remarkably similar between the two ocean models. This indicates that
 529 the differences in OGCM resolution itself may not be the primary driver of the differences in β_h and
 530 β_u . Moreover, this finding (Fig. 10) stands in stark contrast to the large differences in β_h and β_u
 531 identified in the two coupled simulations (Figures 6 and 8).



532
 533 **Figure 10.** (a)–(b) and (c)–(d) are same as Figure 6 and 8, respectively, but for the OMIP2 simulations.

534 To understand the contrasting OMIP–CMIP behavior, we compare the meridional structures of the
 535 “normalized τ_x' ” between the CMIP and OMIP experiments for both model versions, as shown in Figure
 536 S5. Here the normalized τ_x' is obtained by regressing the τ_x' field onto Niño4-region-averaged τ_x' ;
 537 and then averaging over the Niño4 longitude range (160°E–150°W). This normalization procedure
 538 enables a fair comparison of the meridional structure of τ_x' across different experiments and model
 539 versions. In f3-L, the CMIP experiment produces stronger τ_x' near the equator compared to the OMIP
 540 forcing that was derived from the JRA55-do reanalysis (red lines in Fig. S5). This leads to an enhanced
 541 thermocline response in CMIP relative to OMIP. Conversely, in f3-H, the CMIP experiment yields

542 weaker equatorial τ_x' than the OMIP forcing (blue lines in Fig. S5), resulting in a weaker thermocline
 543 response in CMIP relative to OMIP.

544 Table 3. Meridional distribution index (MDI; units: $^\circ$) of τ_x' , calculated from the meridional
 545 structure of normalized τ_x' as shown in Fig. B6.

	f3-L	f3-H
CMIP	2.55	2.71
OMIP	2.68	2.64

546 Furthermore, we quantify these structural differences in τ_x' between the CMIP and OMIP
 547 experiments based on the *MDI* metric, as introduced in section 2.3.3. The qualitative differences in τ_x'
 548 distributions shown in Fig. S5 are corroborated by the *MDI* results (Table 3). In f3-L, the CMIP
 549 experiment yields a notably smaller *MDI* (2.55°) than the OMIP experiment (2.68°), indicating a more
 550 equatorially concentrated τ_x' structure that can more efficiently drive thermocline variability, and hence
 551 produces a larger β_h in the CMIP experiment. Conversely, in f3-H, the CMIP experiment exhibits a larger
 552 *MDI* (2.71°) than the OMIP experiment (2.64°), corresponding to a broader τ_x' distribution that drives
 553 a more moderate thermocline response and a smaller β_h .

554 Therefore, the evidence from the OMIP2 experiments corroborates our main conclusion: the refined
 555 atmospheric horizontal resolution, which more realistically captures the meridional structure of τ_x' , plays
 556 a decisive role in improving the simulation of the key air-sea feedbacks (β_b and β_u) and ENSO
 557 amplitude in FGOALS-f3 model. Nevertheless, a more comprehensive investigation, potentially
 558 involving finer oceanic resolutions and their interactions with the atmosphere, deserves further
 559 exploration in the future.

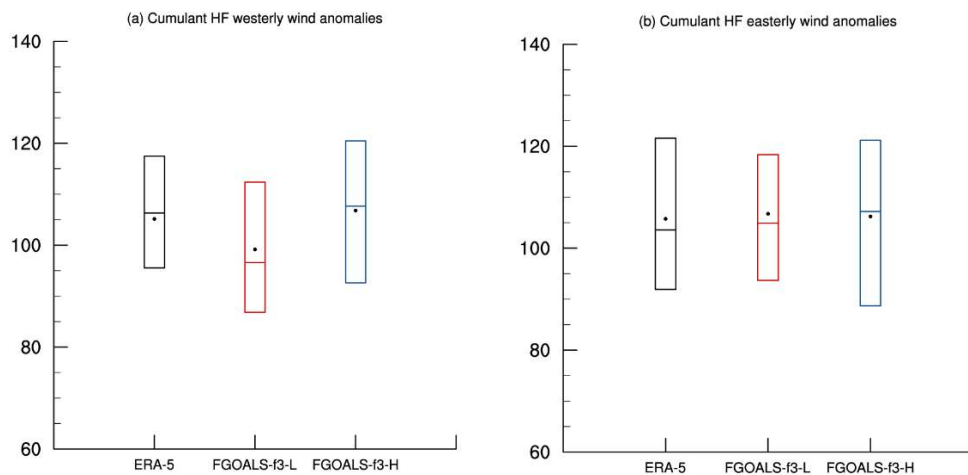
560 **5. Diagnostic of Oscillation Regularity**

561 **5.1 Resolution dependence of ENSO irregularity: Differences in HF wind activity**

562 A large body of studies have suggested that the HF zonal wind activity over the western and central
 563 equatorial Pacific (WCEP) plays a crucial role in the onset and development of ENSO events (Rong et
 564 al., 2011; Chen et al., 2017). In general, this HF zonal wind activity refers to westerly wind event (WWE)
 565 and easterly wind event (EWE) with time scales less than 90 days. Due to their transient, intense, and
 566 somewhat random nature, the HF zonal wind forcing is also considered as an important factor

567 contributing to the diversity and irregularity of ENSO (Chen et al., 2015a; Fedorov et al., 2015).
 568 Motivated by this, we hypothesize that the difference in the ENSO regularity between f3-L and f3-H may
 569 arise from the differences in HF zonal wind activity.

570 To test this, we calculate the intensity of the HF zonal wind activity based on the Equations (14) and
 571 (15). Figure 11 shows the WWI and EWI index that measures the cumulative sum of HF westerly
 572 (easterly) wind anomalies over WCEP during the ENSO development period, for the observation and the
 573 two model versions. As shown in Figure 11a, the intensity of HF westerlies in f3-H is comparable to that
 574 in the observation, with similar mean and median values. However, f3-L simulates much weaker intensity
 575 of HF westerlies. For HF easterly activity (Fig. 11b), both models show comparable statistics to the
 576 observation, with no significant differences between f3-L and f3-H. Overall, these results indicate that
 577 f3-L strongly underestimates HF westerly wind activity relative to the f3-H and the observation.



578
 579 **Figure 11.** The boxplots of the (a) WWI index and (b) EWI index during the ENSO development phase (January to
 580 August). Red, blue and black boxes indicate the f3-L, f3-H and observations, respectively. The upper and lower
 581 boundaries of the box represent the 75th and 25th percentile values, respectively. The horizontal line in the box
 582 represents the median. The black dot represents the average value.

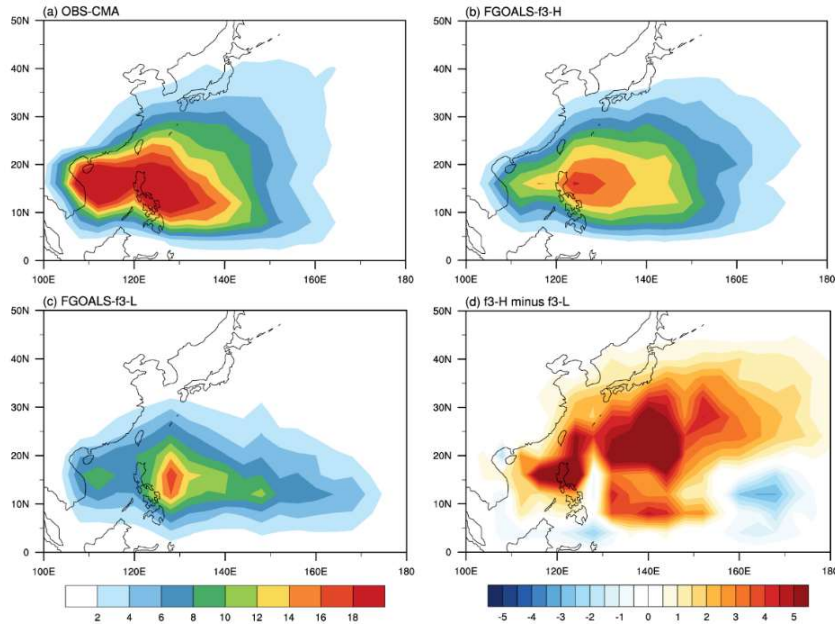
583 HF westerly wind activities are considered as semi-stochastic perturbations that modulate ENSO
 584 evolution (Gebbie et al., 2007; Gebbie and Tziperman, 2009). On the one hand, their occurrence is partly
 585 influenced by ENSO-related SSTA (Sun et al., 2020), but is also regarded as random noise independent
 586 of ENSO system (Moore and Kleeman, 1999). Most ENSO theoretical models treat HF westerly wind
 587 activity as external white noise forcing (Eisenman et al., 2005). This implies that the impact of HF activity
 588 on the coupled system depends, to some extent, on its relative magnitude relative to the ENSO amplitude.
 589 Notably, the aforementioned analysis based on the BJ index (a linear framework that excludes nonlinear

590 processes like atmospheric "noise") has shown that the coupled system simulated by f3-L is more
591 unstable than that of f3-H, hence the ENSO variability in f3-L is more prone to self-sustained oscillation.
592 Considering that the HF wind activities in f3-L is also significantly weaker than that in f3-H, from the
593 perspective of signal-to-noise ratio, this weaker "noise" is insufficient to "disrupt" the overly strong
594 ENSO oscillation in f3-L, allowing its ENSO cycle to evolve in a regular and self-sustained manner.

595 To further quantify the relative magnitude of stochastic atmospheric forcing compared to the ENSO
596 signal, we introduce an *NSR* metric, as introduced in section 2.3.5. A larger *NSR* indicates stronger
597 stochastic forcing relative to the ENSO signal. The *NSR* values are 2.67, 1.98, and 4.73 ($\text{m s}^{-1} \text{K}^{-1}$) for
598 the observation, f3-L, and f3-H, respectively. The substantially smaller *NSR* in f3-L reflects the
599 combination of its weaker HF wind activity and stronger ENSO amplitude, confirming that the stochastic
600 forcing in f3-L is insufficient to disrupt its overly intense ENSO oscillation. In contrast, the larger *NSR*
601 in f3-H indicates that stronger stochastic forcing acts on a weaker ENSO signal, facilitating the irregular
602 oscillation that more closely resembles the observation.

603 **5.2 Sources of differences in HF westerly wind activity: evaluation of TC and MJO**

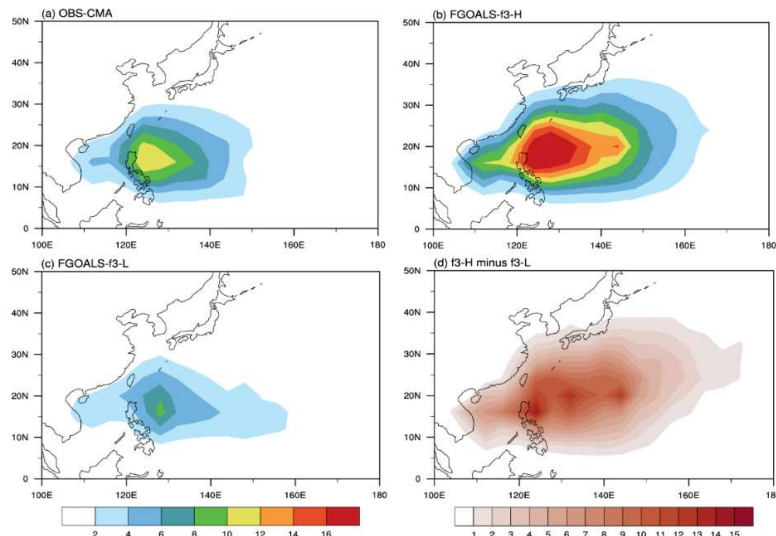
604 To further explore the origin of difference in HF westerly wind intensity between f3-L and f3-H, we
605 compare the simulated performance of TC and MJO activities in these two models. The results show that
606 the differences in the HF westerly wind intensity are primarily related to the models' ability to reproduce
607 TC activity. Figure 12 shows the spatial distribution of TCTD over the western North Pacific (WNP).
608 The spatial distributions of TCTD in both f3-H and f3-L are similar to the observation, with TC tracks
609 primarily located in the southwestern quadrant of WNP. Although both versions can reasonably
610 reproduce the spatial distribution characteristics of TC activities over the WNP, a significant difference
611 exists in TC frequency: TC activity is much more frequent in f3-H than that in f3-L. The difference map
612 (Fig. 12d, f3-H minus f3-L) shows positive values almost everywhere north of the equator. It is worth
613 noting that TCTD in f3-H remains relatively weak compared to the observation, which is a common
614 simulation bias in most current climate models (Nakamura et al., 2017; Tang et al., 2022). Although f3-
615 H still underestimates TC activity compared to the observation, this improvement relative to f3-L is
616 substantial.



617

618 **Figure 12.** The averaged TC track density (TCTD, units: counts year⁻¹) over western North Pacific for (a)
 619 Observation (CMA), (b) f3-H, (c) f3-L and (d) the difference between f3-H and f3-L (f3-H minus f3-L).

620 Furthermore, we compare the difference in the TC intensity between f3-H and f3-L. Figure 13 shows
 621 the spatial distribution of ACE index over WNP in the observation and the models. Both models show
 622 that strong TC activity is primarily concentrated east of the Philippines sea, consistent with the
 623 observation (Ma et al., 2025). However, the ACE index in f3-H is significantly stronger than that in f3-
 624 L, indicating stronger TC activity in f3-H. In summary, the TC activity over WNP is more frequent and
 625 intense in f3-H than that in f3-L, which largely explains the stronger HF westerly wind anomalies in f3-
 626 H.



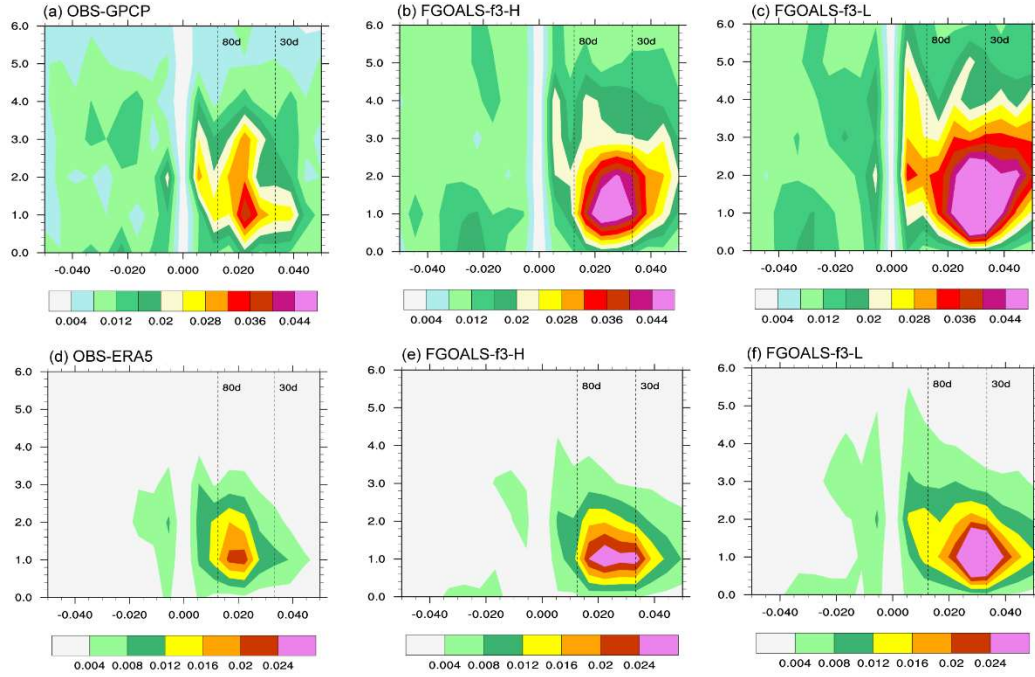
627

628 **Figure 13.** The averaged accumulated cyclone energy (ACE, units: 10⁴ knots year⁻¹) over western North Pacific for
 629 (a) Observation (CMA), (b) f3-H, (c) f3-L and (d) the difference between f3-H and f3-L (f3-H minus f3-L).

630 Model horizontal resolution is a key factor in TC simulation (Tang et al., 2022). In general, climate
631 models with coarse resolutions (≥ 100 km) tend to only reproduce TC-like structures (Camargo et al.,
632 2005; Camargo and Wing, 2016), with activity that is relatively weak and infrequent (Camargo, 2013;
633 Nakamura et al., 2017). As resolution increases, models can simulate more frequent and more intense TC
634 activity (Roberts et al., 2020a; Tang et al., 2022). In particular, when the horizontal resolution is increased
635 to 25 km, the simulation of TC spatial structure and associated wind fields is significantly improved,
636 yielding more realistic characteristics of TC activity (Davis et al., 2018; Roberts et al., 2020b). The
637 analysis results of the FGOALS-f3 models (Figs. 11 and 12) are consistent with these previous findings.
638 Compared to the f3-L model (with a horizontal resolution of 100 km), the f3-H model (with a horizontal
639 resolution of 25 km) provides a more realistic simulation of TC frequency and produces stronger TC
640 intensities. This difference in TC simulation associated with model resolution modulates the intensity of
641 HF westerly wind activity and hence influences the regularity of ENSO cycle in the two models.

642 On the other hand, we also examine the other primary source of HF westerly wind activity—the MJO.
643 Figure 14 shows the wavenumber-frequency spectra of the space-time filtered precipitation and surface
644 zonal wind. It can be seen that the spectral peak of precipitation and surface zonal wind in both models
645 are concentrated at 30-80-day period, consistent with the observation. This indicates that both models
646 reproduce the observed MJO timescales reasonably well. In terms of intensity, although the MJO-related
647 precipitation and zonal wind fields are somewhat exaggerated in both models compared to the
648 observation, the difference between f3-L and f3-H is small, especially for MJO-related zonal winds.
649 Therefore, the difference in HF westerly wind activity is likely not directly linked to MJO activity.

650 Although finer resolution may improve model performance in certain aspects, these preliminary
651 results show no significant improvement in MJO simulation from 100 km to 25 km in the case of these
652 two FGOALS-f3 models. On the one hand, this may be because MJO simulation is heavily constrained
653 by the accurate representation of physical processes like convection parameterization, boundary layer
654 processes, and air-sea coupling. Thus, increased resolution must be combined with optimized physics
655 schemes to effectively improve MJO simulation (Jiang et al., 2020b). On the other hand, recent studies
656 suggest that significant MJO improvement can be seen when resolution increases to the kilometer-scale—
657 the "convection-permitting resolution" (Savarin and Chen, 2022).



658

659 **Figure 14.** Wavenumber-frequency spectra of space-time filtered (a)–(c) precipitation (units: mm/day) and (d)–(f)
 660 surface zonal wind fields (m/s) during the boreal winter (November to next August) for observation (left column),
 661 f3-H (middle column) and f3-L (right column).

662

In summary, we find that the high-resolution version can better simulate TC activity, with more
 663 frequent and stronger TCs over the WNP than the lower-resolution version. This difference results in
 664 stronger HF westerly wind activity in f3-H than that in f3-L. Given that HF westerly wind activity acts
 665 as a stochastic forcing on ENSO, the relatively weaker HF atmospheric noise in f3-L has a limited
 666 randomizing effect on its stronger ENSO signal. In other words, the weaker HF zonal wind activity in
 667 f3-L cannot overcome its inherently stronger ENSO signal, leading to overly regular oscillation in f3-L.
 668 In contrast, f3-H has a weaker intrinsic ENSO signal but stronger "noise". Therefore, the ENSO cycle in
 669 f3-L appears much more regular than that in f3-H.

670

6. Conclusions and implications

671

6.1 Conclusions

672

This study provides a process-based evaluation of how horizontal resolution influences ENSO
 673 simulation in the CAS FGOALS-f3 climate system model. The comparison between its low-resolution
 674 (f3-L, ~100 km) and high-resolution (f3-H, ~25 km) configurations reveals systematic and resolution-
 675 dependent differences in ENSO amplitude, period, oscillation irregularity, and underlying air-sea

676 coupling processes.

677 A key structural source of bias in f3-L is the overly confined meridional structure of ENSO-related
678 zonal wind stress anomalies, which strengthens the thermocline and zonal-advection feedbacks and leads
679 to an exaggerated ENSO amplitude. The process-oriented diagnosis based on ENSO-related air-sea
680 coupling processes demonstrates that these feedbacks can be directly attributed to resolution-sensitive
681 meridional distribution of equatorial zonal wind stress anomalies, indicating that resolving the meridional
682 structure of wind forcing is essential for realistic representation of ENSO amplitude.

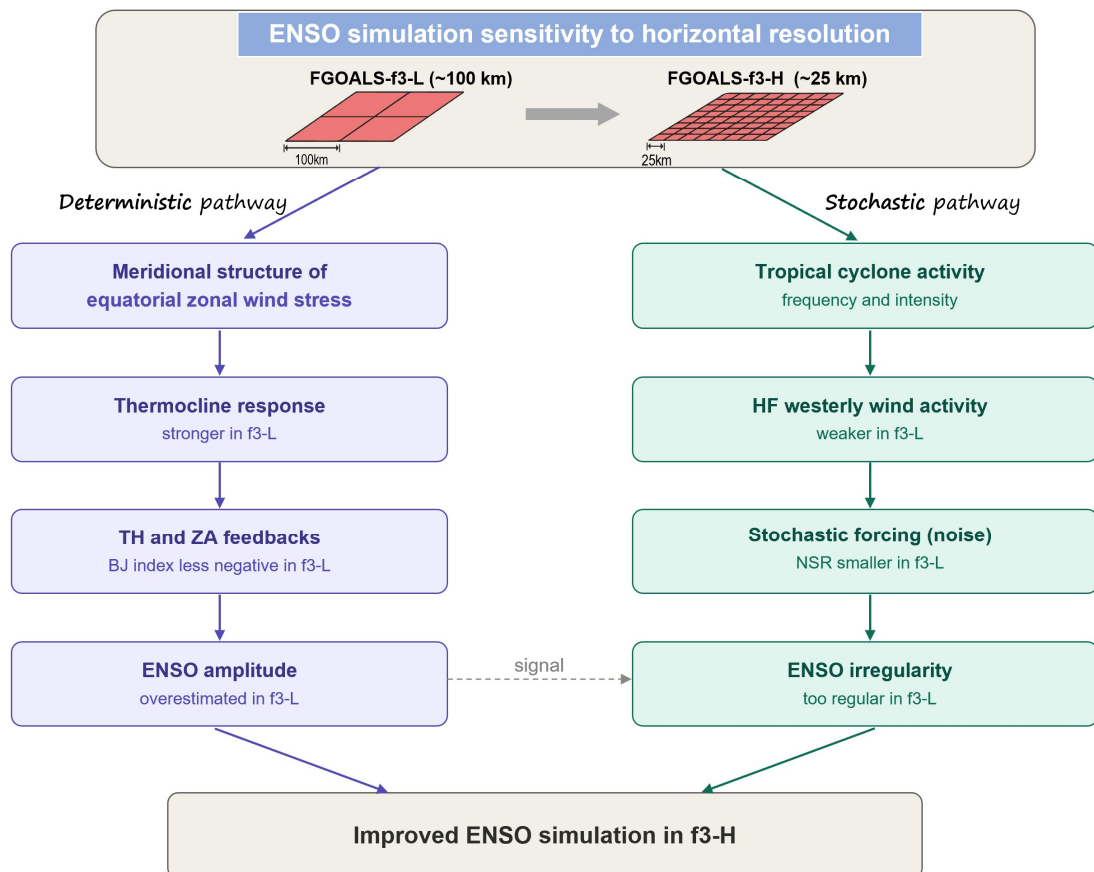
683 The excessive regularity of ENSO in f3-L is another resolution-driven bias, arising from insufficient
684 HF atmospheric variability. The high-resolution configuration produces more realistic TC activity and
685 more vigorous WWEs, which introduce stochastic forcing that disrupts the ENSO cycle and generates
686 irregular variability closer to the observation. These results highlight that the representation of synoptic-
687 scale atmospheric processes is integral to capturing observed temporal irregularity of ENSO.

688 Overall, this study demonstrates that ENSO-related biases in FGOALS-f3 arise from identifiable,
689 resolution-sensitive structural features in the coupled system. Through two complementary diagnostic
690 pathways, we provide a traceable and mechanistic explanation for how horizontal resolution modulates
691 ENSO simulation (Figure 15). The diagnostic framework developed here is model-agnostic and
692 reproducible, offering a practical tool for evaluating ENSO performance in other climate models and
693 guiding future development of the FGOALS-f3 model family.

694 **6.2 Implications**

695 The findings from this study yield several actionable insights for FGOALS-f3 development and for
696 the broader CMIP-class modeling community. (1) Improving the atmospheric representation of
697 equatorial wind stress meridional gradient should be a development priority. (2) As shown in Figure 15,
698 increase in horizontal resolution has impacts on ENSO dynamics from both deterministic and stochastic
699 pathways: the deterministic aspect influencing ENSO behaviors is via air-sea coupling processes, and
700 the stochastic aspect influencing ENSO behaviors is via HF wind activity, both of which should be
701 explicitly considered in future model evaluation framework. (3) The diagnostics applied here are model-
702 agnostic and can serve as a reproducible framework for assessing resolution effects in other climate
703 models participating in CMIP6/CMIP7. We encourage the community to adopt the process-oriented
704 diagnostics presented here as a complement to conventional statistical metrics, so that the improvements

705 in ENSO simulation can be traced back to specific physical mechanisms rather than assessed solely by
 706 outcome-based indices. (4) The ~25 km atmosphere resolution of f3-H improves both the air-sea coupling
 707 processes and the stochastic forcing mechanisms, supporting the ongoing efforts toward next-generation
 708 high-resolution climate models. However, the computational cost increases substantially from f3-L to f3-
 709 H. The low-resolution version runs on 384 processor cores and achieves a throughput of approximately
 710 15–20 model years per wall-clock day, whereas the high-resolution version requires 6,144 processor
 711 cores and achieves only ~0.25 model years per wall-clock day. This sharp increase in computational
 712 expense makes century-scale ensemble simulations with high-resolution models, such as f3-H,
 713 considerably more demanding. Such a cost–benefit trade-off further motivates the development of
 714 variable-resolution modeling frameworks (e.g., the Model for Prediction Across Scales and the
 715 ICOSahedral Nonhydrostatic model), which can selectively refine the grid over the tropical Pacific to
 716 capture these resolution-sensitive processes while maintaining coarser resolution elsewhere.



717
 718 **Figure 15.** Schematic diagram illustrating how increased horizontal resolution (~100 km to ~25 km) improves ENSO
 719 simulation in FGOALS-f3 via both the deterministic feedback processes and the stochastic atmospheric forcing
 720 pathways.

721

722

723 *Data and Code availability.* Source codes of the FGOALS-f3 model used in this study and the analysis
724 scripts are archived at <https://doi.org/10.5281/zenodo.19552337> (Song et al., 2026). The model output of
725 FGOALS-f3 models described in this paper is distributed through the Earth System Grid Federation
726 (ESGF) and is freely obtained via the ESGF data portals after registration (<https://aims2.llnl.gov/search>,
727 last access: 27 November 2025). All the observation and reanalysis datasets are available online and
728 publicly available as cited in the references. The ORAS5 and ERA-5 datasets are obtained from
729 <https://cds.climate.copernicus.eu/datasets>. The HadISST dataset is from
730 <https://www.metoffice.gov.uk/hadobs/hadisst/data/download.html>. The GPCP dataset is available at
731 <https://www.ncei.noaa.gov/data/global-precipitation-climatology-project-gpcp-daily/access>. The
732 SODA2.2.4 dataset can be accessed at http://apdrc.soest.hawaii.edu/datadoc/soda_2.2.4.php. The CMA
733 TC best track dataset is from <https://tcdata.typhoon.org.cn/en/zjljsjj.html>. The description and data for
734 HighResSST-present simulations of FGOALS-f3 can be found at
735 <http://doi.org/10.22033/ESGF/CMIP6.3312> (Bao and He, 2019; Bao et al., 2020).

736 *Author contribution.* All authors contributed to the study conception and design. Material preparation,
737 data collection and analysis were performed by MS and LC. JZ contributed to the application of methods
738 related to TC detection. The first draft of the manuscript was written by MS and LC. QY, BA and HZ
739 discussed the results and commented on the manuscript. All authors read and approved the final
740 manuscript.

741 *Competing interests.* The authors declare that they have no conflict of interest.

742 *Disclaimer.* Publisher's note: Copernicus Publications remains neutral with regard to jurisdictional
743 claims made in the text, published maps, institutional affiliations, or any other geographical
744 representation in this paper. While Copernicus Publications makes every effort to include appropriate
745 place names, the final responsibility lies with the authors. Views expressed in the text are those of the
746 authors and do not necessarily reflect the views of the publisher.

747 *Acknowledgements.* We acknowledge the High Performance Computing Center of Nanjing University of
748 Information Science & Technology for their support of this work.

749 *Financial support.* This work was the jointly supported by the National Key Research and Development
750 Program of China (Grant 2022YFF0802004), NSFC (No. 42576024), the Excellent Youth Natural
751 Science Foundation of Jiangsu Province (BK20230061) and Postgraduate Research & Practice
752 Innovation Program of Jiangsu Province (KYCX24_1417).

753

754 **Reference**

755 Adler, R. F., Huffman, G. J., Chang, A., Ferraro, R., Xie, P.-P., Janowiak, J., Rudolf, B., Schneider, U.,
756 Curtis, S., Bolvin, D., Gruber, A., Susskind, J., Arkin, P., and Nelkin, E.: The version-2 global
757 precipitation climatology project (GPCP) monthly precipitation analysis (1979–present), *Journal of*
758 *Hydrometeorology*, 4, 1147–1167, [https://doi.org/10.1175/1525-](https://doi.org/10.1175/1525-7541(2003)004%3C1147:TVGPCP%3E2.0.CO;2)
759 [7541\(2003\)004%3C1147:TVGPCP%3E2.0.CO;2](https://doi.org/10.1175/1525-7541(2003)004%3C1147:TVGPCP%3E2.0.CO;2), 2003.

760 An, B., Yu, Y. Q., Bao, Q., He, B., Li, J. X., Luan, Y. H., Chen, K. J., and Zheng, W. P.: CAS FGOALS-
761 f3-H dataset for the high-resolution model intercomparison project (HighResMIP) Tier 2, *Advances*
762 *in Atmospheric Sciences*, 39, 1873–1884, <https://doi.org/10.1007/s00376-022-2030-5>, 2022.

763 Bacmeister, J. T., Wehner, M. F., Neale, R. B., Gettelman, A., Hannay, C., Lauritzen, P. H., Caron, J. M.,
764 and Truesdale, J. E.: Exploratory high-resolution climate simulations using the community
765 atmosphere model (CAM), *Journal of Climate*, 27, 3073–3099, [https://doi.org/10.1175/jcli-d-13-](https://doi.org/10.1175/jcli-d-13-00387.1)
766 [00387.1](https://doi.org/10.1175/jcli-d-13-00387.1), 2014.

767 Bao, Q., Liu, Y. M., Wu, G. X., He, B., Li, J. X., Wang, L., Wu, X. F., Chen, K. J., Wang, X. C., Yang, J.,
768 and Zhang, X. Q.: CAS FGOALS-f3-H and CAS FGOALS-f3-L outputs for the high-resolution
769 model intercomparison project simulation of CMIP6, *Atmospheric and Oceanic Science Letters*, 13,
770 576–581, <https://doi.org/10.1080/16742834.2020.1814675>, 2020.

771 Bao, Q. and He, B.: CAS FGOALS-f3-H model output prepared for CMIP6 HighResMIP highresSST-
772 present, Earth System Grid Federation [data set], <https://doi.org/10.22033/ESGF/CMIP6.3312>,
773 2019

774 Barnston, A. G., Tippett, M. K., L'Heureux, M. L., Li, S., and DeWitt, D. G.: Skill of real-time seasonal
775 ENSO model predictions during 2002–11: Is our capability increasing?, *Bulletin of the American*
776 *Meteorological Society*, 93, 631–651, <https://doi.org/10.1175/bams-d-11-00111.1>, 2012.

777 Bell, G. D., Halpert, M. S., Schnell, R. C., Higgins, R. W., Lawrimore, J., Kousky, V. E., Tinker, R.,
778 Thiaw, W., Chelliah, M., and Artusa, A.: Climate assessment for 1999, *Bulletin of the American*
779 *Meteorological Society*, 81, s1–s50, [https://doi.org/10.1175/1520-0477\(2000\)81\[s1:CAF\]2.0.CO;2](https://doi.org/10.1175/1520-0477(2000)81[s1:CAF]2.0.CO;2),
780 2000.

781 Cai, W. J., Santoso, A., Collins, M., Dewitte, B., Karamperidou, C., Kug, J.-S., Lengaigne, M., McPhaden,
782 M. J., Stuecker, M. F., Taschetto, A. S., Timmermann, A., Wu, L. X., Yeh, S.-W., Wang, G., Ng, B.,
783 Jia, F., Yang, Y., Ying, J., Zheng, X.-T., Bayr, T., Brown, J. R., Capotondi, A., Cobb, K. M., Gan, B.,
784 Geng, T., Ham, Y.-G., Jin, F.-F., Jo, H.-S., Li, X., Lin, X., McGregor, S., Park, J.-H., Stein, K., Yang,
785 K., Zhang, L., and Zhong, W. X.: Changing El Niño–Southern Oscillation in a warming climate,
786 *Nature Reviews Earth and Environment*, 2, 628–644, <https://doi.org/10.1038/s43017-021-00199-z>,
787 2021.

788 Camargo, S. J., Barnston, A. G., and Zebiak, S. E.: A statistical assessment of tropical cyclone activity in
789 atmospheric general circulation models, *Tellus A: Dynamic Meteorology and Oceanography*, 57,
790 589–604, <https://doi.org/10.3402/tellusa.v57i4.14705>, 2005.

791 Camargo, S. J.: Global and regional aspects of tropical cyclone activity in the CMIP5 models, *Journal of*
792 *Climate*, 26, 9880–9902, <https://doi.org/10.1175/jcli-d-12-00549.1>, 2013.

793 Camargo, S. J. and Wing, A. A.: Tropical cyclones in climate models, *Wiley Interdisciplinary Reviews:*
794 *Climate Change*, 7, 211–237, <https://doi.org/10.1002/wcc.373>, 2016.

795 Carton, J. A. and Giese, B. S.: A Reanalysis of Ocean Climate Using Simple Ocean Data Assimilation
796 (SODA), *Monthly Weather Review*, 136, 2999–3017, <https://doi.org/10.1175/2007mwr1978.1>,
797 2008.

798 Chang, P., Zhang, S. Q., Danabasoglu, G., Yeager, S. G., Fu, H. H., Wang, H., Castruccio, F. S., Chen,
799 Y., Edwards, J., Fu, D., Jia, Y., Laurindo, L. C., Liu, X., Rosenbloom, N., Small, R. J., Xu, G. P.,
800 Zeng, Y. H., Zhang, Q. Y., Bacmeister, J., Bailey, D. A., Duan, X., DuVivier, A. K., Li, D. P., Li, Y.
801 X., Neale, R., Stössel, A., Wang, L., Zhuang, Y., Baker, A., Bates, S., Dennis, J., Diao, X., Gan, B.
802 L., Gopal, A., Jia, D. N., Jing, Z., Ma, X., Saravanan, R., Strand, W. G., Tao, J., Yang, H. Y., Wang,
803 X. Q., Wei, Z. Q., and Wu, L. X.: An unprecedented set of high-resolution earth system simulations
804 for understanding multiscale interactions in climate variability and change, *Journal of Advances in*
805 *Modeling Earth Systems*, 12, e2020MS002298, <https://doi.org/10.1029/2020ms002298>, 2020.

806 Chen, D. K., Lian, T., Fu, C., Cane, M. A., Tang, Y. M., Murtugudde, R., Song, X. S., Wu, Q. Y., and
807 Zhou, L.: Strong influence of westerly wind bursts on El Niño diversity, *Nature Geoscience*, 8, 339–
808 345, <https://doi.org/10.1038/ngeo2399>, 2015a.

809 Chen, L., Li, T., and Yu, Y. Q.: Causes of strengthening and weakening of ENSO amplitude under global
810 warming in four CMIP5 models, *Journal of Climate*, 28, 3250–3274, [https://doi.org/10.1175/jcli-d-](https://doi.org/10.1175/jcli-d-14-00439.1)
811 14-00439.1, 2015b.

812 Chen, L., Yu, Y. Q., and Zheng, W. P.: Improved ENSO simulation from climate system model FGOALS-
813 g1.0 to FGOALS-g2, *Climate Dynamics*, 47, 2617–2634, [https://doi.org/10.1007/s00382-016-](https://doi.org/10.1007/s00382-016-2988-8)
814 2988-8, 2016a.

815 Chen, L., Li, T., Behera, S. K., and Doi, T.: Distinctive precursory air–sea signals between regular and
816 super El Niños, *Advances in Atmospheric Sciences*, 33, 996–1004, [https://doi.org/10.1007/s00376-](https://doi.org/10.1007/s00376-016-5250-8)
817 016-5250-8, 2016b.

818 Chen, L., Li, T., Wang, B., and Wang, L.: Formation mechanism for 2015/16 super El Nino, *Scientific*
819 *Reports*, 7, 2975–2985, <https://doi.org/10.1038/s41598-017-02926-3>, 2017.

820 Chen, L., Wang, L., Li, T., and Liu, J.: Drivers of reduced ENSO variability in mid-Holocene in a coupled
821 model, *Climate Dynamics*, 52, 5999–6014, <https://doi.org/10.1007/s00382-018-4496-5>, 2019a.

822 Chen, L., Zheng, W., and Braconnot, P.: Towards understanding the suppressed ENSO activity during
823 mid-Holocene in PMIP2 and PMIP3 simulations, *Climate Dynamics*, 53, 1095-1110,
824 <https://doi.org/10.1007/s00382-019-04637-z>, 2019b.

825 Craig, A. P., Vertenstein, M., and Jacob, R.: A new flexible coupler for earth system modeling developed
826 for CCSM4 and CESM1, *The International Journal of High Performance Computing Applications*,
827 26, 31–42, <https://doi.org/10.1177/1094342011428141>, 2012.

828 Davis, C. A.: Resolving tropical cyclone intensity in models, *Geophysical Research Letters*, 45, 2082–
829 2087, <https://doi.org/10.1002/2017GL076966>, 2018.

830 Dawson, A., Matthews, A. J., Stevens, D. P., Roberts, M. J., and Vidale, P. L.: Importance of oceanic
831 resolution and mean state on the extra-tropical response to El Niño in a matrix of coupled models,
832 *Climate Dynamics*, 41, 1439–1452, <https://doi.org/10.1007/s00382-012-1518-6>, 2013.

833 Docquier, D., Grist, J. P., Roberts, M. J., Roberts, C. D., Semmler, T., Ponsoni, L., Massonnet, F.,
834 Sidorenko, D., Sein, D. V., Iovino, D., Bellucci, A., and Fichet, T.: Impact of model resolution on

835 Arctic sea ice and North Atlantic Ocean heat transport, *Climate Dynamics*, 53, 4989–5017,
836 <https://doi.org/10.1007/s00382-019-04840-y>, 2019.

837 Eisenman, I., Yu, L. S., and Tziperman, E.: Westerly wind bursts: ENSO’s tail rather than the dog?,
838 *Journal of Climate*, 18, 5224–5237, <https://doi.org/10.1175/JCLI3588.1>, 2005.

839 Eyring, V., Bony, S., Meehl, G. A., Senior, C. A., Stevens, B., Stouffer, R. J., and Taylor, K. E.: Overview
840 of the Coupled Model Intercomparison Project Phase 6 (CMIP6) experimental design and
841 organization, *Geoscientific Model Development*, 9, 1937–1958, [https://doi.org/10.5194/gmd-9-](https://doi.org/10.5194/gmd-9-1937-2016)
842 [1937-2016](https://doi.org/10.5194/gmd-9-1937-2016), 2016.

843 Fedorov, A. V.: The response of the coupled tropical ocean–atmosphere to westerly wind bursts,
844 *Quarterly Journal of the Royal Meteorological Society*, 128, 1–23,
845 <https://doi.org/10.1002/qj.200212857901>, 2002.

846 Fedorov, A. V., Hu, S. N., Lengaigne, M., and Guilyardi, E.: The impact of westerly wind bursts and
847 ocean initial state on the development, and diversity of El Niño events, *Climate Dynamics*, 44,
848 1381–1401, <https://doi.org/10.1007/s00382-014-2126-4>, 2015.

849 Gebbie, G., Eisenman, I., Wittenberg, A., and Tziperman, E.: Modulation of westerly wind bursts by sea
850 surface temperature: A semistochastic feedback for ENSO, *Journal of the Atmospheric Sciences*, 64,
851 3281–3295, <https://doi.org/10.1175/jas4029.1>, 2007.

852 Gebbie, G. and Tziperman, E.: Incorporating a semi-stochastic model of ocean-modulated westerly wind
853 bursts into an ENSO prediction model, *Theoretical and Applied Climatology*, 97, 65–73,
854 <https://doi.org/10.1007/s00704-008-0069-6>, 2009.

855 Griffies, S. M., Danabasoglu, G., Durack, P. J., Adcroft, A. J., Balaji, V., Böning, C. W., Chassignet, E.
856 P., Curchitser, E., Deshayes, J., Drange, H., Fox-Kemper, B., Gleckler, P. J., Gregory, J. M., Haak,
857 H., Hallberg, R. W., Heimbach, P., Hewitt, H. T., Holland, D. M., Ilyina, T., Jungclaus, J. H., Komuro,
858 Y., Krasting, J. P., Large, W. G., Marsland, S. J., Masina, S., McDougall, T. J., Nurser, A. J. G., Orr,
859 J. C., Pirani, A., Qiao, F. I., Stouffer, R. J., Taylor, K. E., Treguier, A. M., Tsujino, H., Uotila, P.,
860 Valdivieso, M., Wang, Q., Winton, M., and Yeager, S. G.: OMIP contribution to CMIP6:
861 experimental and diagnostic protocol for the physical component of the Ocean Model
862 Intercomparison Project, *Geoscientific Model Development*, 9, 3231–3296,
863 <https://doi.org/10.5194/gmd-9-3231-2016>, 2016.

864 Guilyardi, E., Gualdi, S., Slingo, J., Navarra, A., Delecluse, P., Cole, J., Madec, G., Roberts, M., Latif,
865 M., and Terray, L.: Representing El Niño in coupled ocean–atmosphere GCMs: The dominant role
866 of the atmospheric component, *Journal of Climate*, 17, 4623–4629, [https://doi.org/10.1175/JCLI-](https://doi.org/10.1175/JCLI-3260.1)
867 3260.1, 2004.

868 Guilyardi, E., Capotondi, A., Lengaigne, M., Thual, S., and Wittenberg, A. T.: ENSO modeling: History,
869 progress, and challenges, in: *El Niño Southern Oscillation in a Changing Climate*, edited by:
870 McPhaden, M. J., Santoso, A., and Cai, W., American Geophysical Union, American, 199–226,
871 <https://doi.org/10.1002/9781119548164.ch9>, 2020.

872 Hallberg, R.: Using a resolution function to regulate parameterizations of oceanic mesoscale eddy effects,
873 *Ocean Modelling*, 72, 92–103, <https://doi.org/10.1016/j.ocemod.2013.08.007>, 2013.

874 Harrison, D. E. and Vecchi, G. A.: Westerly wind events in the tropical Pacific, 1986–95*, *Journal of*
875 *Climate*, 10, 3131–3156, [https://doi.org/10.1175/1520-0442\(1997\)010<3131:Wweitt>2.0.Co;2](https://doi.org/10.1175/1520-0442(1997)010<3131:Wweitt>2.0.Co;2),
876 1997.

877 He, B., Bao, Q., Wang, X. C., Zhou, L. J., Wu, X. F., Liu, Y. M., Wu, G. X., Chen, K. J., He, S. C., Hu,
878 W. T., Li, J. D., Li, J. X., Nian, G. K., Wang, L., Yang, J., Zhang, M. H., and Zhang, X. Q.: CAS
879 FGOALS-f3-L model datasets for CMIP6 historical atmospheric model intercomparison project
880 simulation, *Advances in Atmospheric Sciences*, 36, 771–778, [https://doi.org/10.1007/s00376-019-](https://doi.org/10.1007/s00376-019-9027-8)
881 9027-8, 2019.

882 He, B., He, X. Y., Liu, Y. M., Wu, G. X., Bao, Q., Hu, W. T., Sheng, C., and Feng, S. J.: Role of thermal
883 and dynamical subdaily perturbations over the Tibetan Plateau in 30-day extended-range forecast
884 of East Asian precipitation in early summer, *npj Climate and Atmospheric Science*, 8,
885 <https://doi.org/10.1038/s41612-025-00931-2>, 2025a.

886 He, X.-Y., He, B., Bao, Q., Liu, Y.-M., Li, J.-D., Wang, X.-C., Chen, X.-C., and Wu, G.-X.: The sensitivity
887 of the Asian summer monsoon simulation to horizontal resolution and air–sea coupling in the
888 FGOALS-f climate system model, *Advances in Climate Change Research*, 16, 44 – 57,
889 <https://doi.org/10.1016/j.accre.2025.01.008>, 2025b.

890 Hersbach, H., Bell, B., Berrisford, P., Hirahara, S., Horányi, A., Muñoz-Sabater, J., Nicolas, J., Peubey,
891 C., Radu, R., Schepers, D., Simmons, A., Soci, C., Abdalla, S., Abellan, X., Balsamo, G., Bechtold,
892 P., Biavati, G., Bidlot, J., Bonavita, M., De Chiara, G., Dahlgren, P., Dee, D., Diamantakis, M.,

893 Dragani, R., Flemming, J., Forbes, R., Fuentes, M., Geer, A., Haimberger, L., Healy, S., Hogan, R.
894 J., Hólm, E., Janisková, M., Keeley, S., Laloyaux, P., Lopez, P., Lupu, C., Radnoti, G., de Rosnay,
895 P., Rozum, I., Vamborg, F., Villaume, S., and Thépaut, J. N.: The ERA5 global reanalysis, *Quarterly*
896 *Journal of the Royal Meteorological Society*, 146, 1999–2049, <https://doi.org/10.1002/qj.3803>,
897 2020.

898 Hewitt, H. T., Roberts, M. J., Hyder, P., Graham, T., Rae, J., Belcher, S. E., Bourdallé-Badie, R., Copsey,
899 D., Coward, A., Guiavarch, C., Harris, C., Hill, R., Hirschi, J. J. M., Madec, G., Mizielinski, M. S.,
900 Neining, E., New, A. L., Rioual, J.-C., Sinha, B., Storkey, D., Shelly, A., Thorpe, L., and Wood,
901 R. A.: The impact of resolving the Rossby radius at mid-latitudes in the ocean: results from a high-
902 resolution version of the Met Office GC2 coupled model, *Geoscientific Model Development*, 9,
903 3655–3670, <https://doi.org/10.5194/gmd-9-3655-2016>, 2016.

904 Hua, L. J., Chen, L., Rong, X. Y., Su, J. Z., Wang, L., Li, T., and Yu, Y. Q.: Impact of atmospheric model
905 resolution on simulation of ENSO feedback processes: a coupled model study, *Climate Dynamics*,
906 51, 3077–3092, <https://doi.org/10.1007/s00382-017-4066-2>, 2018.

907 Hunke, E. C. and Lipscomb, W. H.: CICE: The Los Alamos Sea Ice Model, Documentation and Software
908 User’s Manual, Version 4.1, Tech. Rep. LA-CC-06-012, Los Alamos National Laboratory, Los
909 Alamos, New Mexico, available at: <http://oceans11.lanl.gov/trac/CICE>, 2010.

910 Jiang, W. P., Huang, P., Li, G., and Huang, G.: Emergent constraint on the frequency of central Pacific
911 El Niño under global warming by the equatorial Pacific cold tongue bias in CMIP5/6 models,
912 *Geophysical Research Letters*, 47, <https://doi.org/10.1029/2020gl089519>, 2020a.

913 Jiang, W. P., Huang, P., Huang, G., and Ying, J.: Origins of the excessive westward extension of ENSO
914 SST simulated in CMIP5 and CMIP6 models, *Journal of Climate*, 34, 2839–2851,
915 <https://doi.org/10.1175/jcli-d-20-0551.1>, 2021.

916 Jiang, X. N., Adames, Á. F., Kim, D., Maloney, E. D., Lin, H., Kim, H., Zhang, C. D., DeMott, C. A.,
917 and Klingaman, N. P.: Fifty years of research on the Madden-Julian Oscillation: Recent progress,
918 challenges, and perspectives, *Journal of Geophysical Research: Atmospheres*, 125,
919 <https://doi.org/10.1029/2019jd030911>, 2020b.

920 Jin, F.-F.: An equatorial ocean recharge paradigm for ENSO. Part I: Conceptual model, *Journal of the*
921 *Atmospheric Sciences*, 54, 811–829, [39](https://doi.org/10.1175/1520-</p></div><div data-bbox=)

922 0469(1997)054<0811:Aeorpf>2.0.Co;2, 1997.

923 Jin, F. F., Kim, S. T., and Bejarano, L.: A coupled-stability index for ENSO, *Geophysical Research Letters*,
924 33, <https://doi.org/10.1029/2006gl027221>, 2006.

925 Kim, S. T. and Jin, F.-F.: An ENSO stability analysis. Part II: Results from the twentieth and twenty-first
926 century simulations of the CMIP3 models, *Climate Dynamics*, 36, 1609–1627,
927 <https://doi.org/10.1007/s00382-010-0872-5>, 2011a.

928 Kim, S. T. and Jin, F.-F.: An ENSO stability analysis. Part I: results from a hybrid coupled model, *Climate*
929 *Dynamics*, 36, 1593–1607, <https://doi.org/10.1007/s00382-010-0796-0>, 2011b.

930 Kreussler, P., Caron, L. P., Wild, S., Loosveldt Tomas, S., Chauvin, F., Moine, M. P., Roberts, M. J.,
931 Ruprich-Robert, Y., Seddon, J., Valcke, S., Vannière, B., and Vidale, P. L.: Tropical cyclone
932 integrated kinetic energy in an ensemble of HighResMIP simulations, *Geophysical Research Letters*,
933 48, <https://doi.org/10.1029/2020gl090963>, 2021.

934 Lawrence, D. M., Oleson, K. W., Flanner, M. G., Thornton, P. E., Swenson, S. C., Lawrence, P. J., Zeng,
935 X., Yang, Z. L., Levis, S., and Sakaguchi, K.: Parameterization improvements and functional and
936 structural advances in version 4 of the Community Land Model, *Journal of Advances in Modeling*
937 *Earth Systems*, 3, <https://doi.org/10.1029/2011MS00045>, 2011.

938 Li, J., Yu, Y. Q., and Sun, D. Z.: Asymmetric Responses in the Equatorial Pacific to Wind Forcing in
939 OMIP2 Experiments: Role of Zonal Currents, *Geophysical Research Letters*, 52, e2025GL114661,
940 <https://doi.org/10.1029/2025gl114661>, 2025.

941 Li, J. X., Bao, Q., Liu, Y. M., Wang, L., Yang, J., Wu, G. X., Wu, X. F., He, B., Wang, X. C., Zhang, X.
942 Q., Yang, Y. X., and Shen, Z. L.: Effect of horizontal resolution on the simulation of tropical
943 cyclones in the Chinese Academy of Sciences FGOALS-f3 climate system model, *Geoscientific*
944 *Model Development*, 14, 6113–6133, <https://doi.org/10.5194/gmd-14-6113-2021>, 2021.

945 Li, T.: Phase transition of the El Niño–Southern Oscillation: A stationary SST mode, *Journal of the*
946 *atmospheric sciences*, 54, 2872–2887, [https://doi.org/10.1175/1520-0469\(1997\)054<2872:PTOTEN>2.0.CO;2](https://doi.org/10.1175/1520-0469(1997)054<2872:PTOTEN>2.0.CO;2), 1997.

948 Li, T. Y., Yu, Y. Q., An, B., Luan, Y. H., and Chen, K. J.: Tropical instability waves in a high-resolution
949 oceanic and coupled GCM, *Ocean Modelling*, 182, <https://doi.org/10.1016/j.ocemod.2023.102169>,
950 2023.

951 Li, Y., Liu, H., Ding, M., Lin, P., Yu, Z., Yu, Y., Meng, Y., Li, Y., Jian, X., and Jiang, J.: Eddy-resolving
952 simulation of CAS-LICOM3 for phase 2 of the ocean model intercomparison project, *Advances in*
953 *Atmospheric Sciences*, 37, 1067–1080, <https://doi.org/10.1007/s00376-020-0057-z>, 2020.

954 Liang, Y. and Fedorov, A. V.: Linking the Madden–Julian Oscillation, tropical cyclones and westerly
955 wind bursts as part of El Niño development, *Climate Dynamics*, 57, 1039–1060,
956 <https://doi.org/10.1007/s00382-021-05757-1>, 2021.

957 Liao, H. X., Cai, Z. C., Guo, J. S., and Song, Z. Y.: Effects of ITCZ poleward location bias on ENSO
958 seasonal phase-locking simulation in climate models, *Journal of Climate*, 36, 5233–5249,
959 <https://doi.org/10.1175/jcli-d-22-0891.1>, 2023.

960 Lu, B., Jin, F.-F., and Ren, H.-L.: A coupled dynamic index for ENSO periodicity, *Journal of Climate*,
961 31, 2361–2376, <https://doi.org/10.1175/jcli-d-17-0466.1>, 2018.

962 Lu, X. Q., Yu, H., Ying, M., Zhao, B. K., Zhang, S., Lin, L. M., Bai, L. N., and Wan, R. J.: Western north
963 Pacific tropical cyclone database created by the China Meteorological Administration, *Advances in*
964 *Atmospheric Sciences*, 38, 690–699, <https://doi.org/https://10.1007/s00376-020-0211-7>, 2021.

965 Ma, T., Yu, W.-D., Speich, S., Zhao, H.-K., Xin, R., Luo, H., and Wu, L.-G.: Philippine archipelago and
966 South China Sea monsoon plus ocean cooling buffer Northwestern Pacific super typhoons, *Nature*
967 *Communications*, 16, <https://doi.org/10.1038/s41467-025-62334-4>, 2025.

968 Madden, R. A. and Julian, P. R.: Detection of a 40–50 day oscillation in the zonal wind in the tropical
969 Pacific, *Journal of Atmospheric Sciences*, 28, 702–708, [https://doi.org/10.1175/1520-0469\(1971\)028%3C0702:DOADOI%3E2.0.CO;2](https://doi.org/10.1175/1520-0469(1971)028%3C0702:DOADOI%3E2.0.CO;2), 1971.

971 Madden, R. A. and Julian, P. R.: Description of global-scale circulation cells in the tropics with a 40–50
972 day period, *Journal of Atmospheric Sciences*, 29, 1109–1123, [https://doi.org/10.1175/1520-0469\(1972\)029%3C1109:DOGSCC%3E2.0.CO;2](https://doi.org/10.1175/1520-0469(1972)029%3C1109:DOGSCC%3E2.0.CO;2), 1972.

974 McPhaden, M. J., Zebiak, S. E., and Glantz, M. H.: ENSO as an integrating concept in earth science,
975 *Science*, 314, 1740–1745, <https://doi.org/10.1126/science.1132588>, 2006.

976 Moore, A. M. and Kleeman, R.: Stochastic forcing of ENSO by the intraseasonal oscillation, *Journal of*
977 *Climate*, 12, 1199–1220, [https://doi.org/10.1175/1520-0442\(1999\)012<1199:Sfoebt>2.0.Co;2](https://doi.org/10.1175/1520-0442(1999)012<1199:Sfoebt>2.0.Co;2),
978 1999.

979 Nakamura, J., Camargo, S. J., Sobel, A. H., Henderson, N., Emanuel, K. A., Kumar, A., LaRow, T. E.,

980 Murakami, H., Roberts, M. J., Scoccimarro, E., Vidale, P. L., Wang, H., Wehner, M. F., and Zhao,
981 M.: Western North Pacific Tropical Cyclone Model Tracks in Present and Future Climates, *Journal*
982 *of Geophysical Research: Atmospheres*, 122, 9721–9744, <https://doi.org/10.1002/2017jd027007>,
983 2017.

984 Navarra, A., Gualdi, S., Masina, S., Behera, S., Luo, J. J., Masson, S., Guilyardi, E., Delecluse, P., and
985 Yamagata, T.: Atmospheric horizontal resolution affects tropical climate variability in coupled
986 models, *Journal of Climate*, 21, 730–750, <https://doi.org/10.1175/2007jcli1406.1>, 2008.

987 Planton, Y. Y., Guilyardi, E., Wittenberg, A. T., Lee, J., Gleckler, P. J., Bayr, T., McGregor, S., McPhaden,
988 M. J., Power, S., Roehrig, R., Vialard, J., and Voldoire, A.: Evaluating climate models with the
989 CLIVAR 2020 ENSO metrics package, *Bulletin of the American Meteorological Society*, 102,
990 E193–E217, <https://doi.org/10.1175/bams-d-19-0337.1>, 2021.

991 Rayner, N. A., Parker, D. E., Horton, E. B., Folland, C. K., Alexander, L. V., Rowell, D. P., Kent, E. C.,
992 and Kaplan, A.: Global analyses of sea surface temperature, sea ice, and night marine air
993 temperature since the late nineteenth century, *Journal of Geophysical Research: Atmospheres*, 108,
994 <https://doi.org/10.1029/2002jd002670>, 2003.

995 Roberts, M. J., Camp, J., Seddon, J., Vidale, P. L., Hodges, K., Vanniere, B., Mecking, J., Haarsma, R.,
996 Bellucci, A., Scoccimarro, E., Caron, L.-P., Chauvin, F., Terray, L., Valcke, S., Moine, M.-P.,
997 Putrasahan, D., Roberts, C., Senan, R., Zarzycki, C., and Ullrich, P.: Impact of model resolution on
998 tropical cyclone simulation using the HighResMIP–PRIMAVERA multimodel ensemble, *Journal*
999 *of Climate*, 33, 2557–2583, <https://doi.org/10.1175/jcli-d-19-0639.1>, 2020a.

1000 Roberts, M. J., Camp, J., Seddon, J., Vidale, P. L., Hodges, K., Vannière, B., Mecking, J., Haarsma, R.,
1001 Bellucci, A., Scoccimarro, E., Caron, L. P., Chauvin, F., Terray, L., Valcke, S., Moine, M. P.,
1002 Putrasahan, D., Roberts, C. D., Senan, R., Zarzycki, C., Ullrich, P., Yamada, Y., Mizuta, R., Kodama,
1003 C., Fu, D., Zhang, Q., Danabasoglu, G., Rosenbloom, N., Wang, H., and Wu, L.: Projected future
1004 changes in tropical cyclones using the CMIP6 HighResMIP multimodel ensemble, *Geophysical*
1005 *Research Letters*, 47, e2020GL088662, <https://doi.org/10.1029/2020gl088662>, 2020b.

1006 Roberts, M. J., Reed, K. A., Bao, Q., Barsugli, J. J., Camargo, S. J., Caron, L.-P., Chang, P., Chen, C.-T.,
1007 Christensen, H. M., Danabasoglu, G., Frenger, I., Fučkar, N. S., ul Hasson, S., Hewitt, H. T., Huang,
1008 H., Kim, D., Kodama, C., Lai, M., Leung, L.-Y. R., Mizuta, R., Nobre, P., Ortega, P., Paquin, D.,

1009 Roberts, C. D., Scoccimarro, E., Seddon, J., Treguier, A. M., Tu, C.-Y., Ullrich, P. A., Vidale, P. L.,
1010 Wehner, M. F., Zarzycki, C. M., Zhang, B., Zhang, W., and Zhao, M.: High-Resolution model
1011 intercomparison project phase 2 (HighResMIP2) towards CMIP7, *Geoscientific Model*
1012 *Development*, 18, 1307–1332, <https://doi.org/10.5194/gmd-18-1307-2025>, 2025.

1013 Rong, X. Y., Zhang, R. H., Li, T., and Su, J. Z.: Upscale feedback of high-frequency winds to ENSO,
1014 *Quarterly Journal of the Royal Meteorological Society*, 137, 894–907,
1015 <https://doi.org/10.1002/qj.804>, 2011.

1016 Savarin, A. and Chen, S. S.: Pathways to better prediction of the MJO:1. Effects of model resolution and
1017 moist physics on Atmospheric boundary layer and precipitation, *Journal of Advances in Modeling*
1018 *Earth Systems*, 14, e2021MS002928, <https://doi.org/10.1029/2021ms002929>, 2022.

1019 Small, R. J., Bryan, F. O., Bishop, S. P., and Tomas, R. A.: Air–Sea turbulent heat fluxes in climate models
1020 and observational analyses: What drives their variability?, *Journal of Climate*, 32, 2397–2421,
1021 <https://doi.org/10.1175/jcli-d-18-0576.1>, 2019.

1022 Song, M.: The code of FGOALS-f3 model study, Zenodo [code],
1023 <https://doi.org/10.5281/zenodo.17778266>, 2025.

1024 Su, J. Z., Zhang, R. H., Li, T., Rong, X. Y., Kug, J. S., and Hong, C.-C.: Causes of the El Niño and La
1025 Niña amplitude asymmetry in the equatorial eastern Pacific, *Journal of Climate*, 23, 605–617,
1026 <https://doi.org/10.1175/2009jcli2894.1>, 2010.

1027 Su, J. Z., Li, T., and Zhang, R. H.: The initiation and developing mechanisms of central Pacific El Niños,
1028 *Journal of Climate*, 27, 4473–4485, <https://doi.org/10.1175/jcli-d-13-00640.1>, 2014.

1029 Sun, M., Li, T., and Chen, L.: El Niño phase-dependent high-frequency variability in western equatorial
1030 Pacific, *Climate Dynamics*, 55, 2165–2184, <https://doi.org/10.1007/s00382-020-05376-2>, 2020.

1031 Tang, Y. L., HuangFu, J. l., Huang, R. H., and Chen, W.: Simulation and projection of tropical cyclone
1032 activities over the western North Pacific by CMIP6 HighResMIP, *Climate Dynamics*, 35, 7771–
1033 7794, <https://doi.org/10.1175/JCLI-D-21-0760.1>, 2022.

1034 Thomson, D. J.: Spectrum estimation and harmonic analysis, *Proceedings of the IEEE*, 79, 1055-1096,
1035 <https://doi.org/10.1109/PROC.1982.12433>, 1982.

1036 Timmermann, A., An, S. I., Kug, J. S., Jin, F. F., Cai, W., Capotondi, A., Cobb, K. M., Lengaigne, M.,
1037 McPhaden, M. J., Stuecker, M. F., Stein, K., Wittenberg, A. T., Yun, K. S., Bayr, T., Chen, H. C.,

1038 Chikamoto, Y., Dewitte, B., Dommenges, D., Grothe, P., Guilyardi, E., Ham, Y. G., Hayashi, M.,
1039 Ineson, S., Kang, D., Kim, S., Kim, W., Lee, J. Y., Li, T., Luo, J. J., McGregor, S., Planton, Y., Power,
1040 S., Rashid, H., Ren, H. L., Santoso, A., Takahashi, K., Todd, A., Wang, G., Wang, G., Xie, R., Yang,
1041 W. H., Yeh, S. W., Yoon, J., Zeller, E., and Zhang, X.: El Niño-Southern Oscillation complexity,
1042 *Nature*, 559, 535–545, <https://doi.org/10.1038/s41586-018-0252-6>, 2018.

1043 Wang, L., Li, T., and Zhou, T. J.: Intraseasonal SST variability and air-sea interaction over the Kuroshio
1044 extension region during boreal summer. *Journal of Climate*, 25, 1619–1634,
1045 <https://doi.org/10.1175/JCLI-D-11-00109.1>, 2012.

1046 Wei, X. J. Chen, L., and Sun, M.: Fine-tuning Atmospheric Parameters for Improving ENSO Simulation
1047 in the Zebiak–Cane Model, *Advances in Atmospheric Science*, 43, 420–435,
1048 <https://doi.org/10.1007/s00376-025-4423-8>, 2026.

1049 Yan, Y. and Sun, D.-Z.: Phase-Locking of El Niño and La Niña events in CMIP6 models, *Atmosphere*,
1050 15, 882, <https://doi.org/10.3390/atmos15080882>, 2024.

1051 Ying, J., Lian, T., Ren, H.-L., Zhang, C., Liu, T., and Tan, X.-X.: Effects of tropical cyclones on ENSO,
1052 *Journal of Climate*, 32, 6423–6443, <https://doi.org/10.1175/jcli-d-18-0821.1>, 2019.

1053 Ying, M., Zhang, W., Yu, H., Lu, X. Q., Feng, J. X., Fan, Y. X., Zhu, Y. t., and Chen, D. Q.: An overview
1054 of the China Meteorological Administration tropical cyclone database, *Journal of Atmospheric and*
1055 *Oceanic Technology*, 31, 287–301, <https://doi.org/https://10.1175/JTECH-D-12-00119.1>, 2014.

1056 Yu, Y. Q., An, B., Liu, H. L., Bao, Q., Lin, P. F., He, B., Zheng, W. P., Luan, Y. H., Bai, R. and Li, T. Y.:
1057 Review of the development and application of the high-resolution climate system model FGOALS,
1058 *Chinese Journal of Atmospheric Sciences (in Chinese)*, 48, 200–217,
1059 <https://doi.org/10.1007/BF02915571>, 2024.

1060 Yu, Y. Q., Tang, S. L., Liu, H. L., Lin, P. F., and Li, X. L.: Development and evaluation of the dynamic
1061 framework of an ocean general circulation model with arbitrary orthogonal curvilinear coordinate,
1062 *Chinese Journal of Atmospheric Sciences (in Chinese)*, 42, 877–889,
1063 <https://doi.org/10.3878/j.issn.1006-9895.1805.17284>, 2018.

1064 Zhang, R.-H., Yu, Y. Q., Song, Z. Y., Ren, H.-L., Tang, Y. M., Qiao, F. l., Wu, T. W., Gao, C., Hu, J. Y.,
1065 Tian, F., Zhu, Y. C., Chen, L., Liu, H. L., Lin, P. F., Wu, F. H., and Wang, L.: A review of progress
1066 in coupled ocean-atmosphere model developments for ENSO studies in China, *Journal of*

1067 Oceanology and Limnology, 38, 930–961, <https://doi.org/10.1007/s00343-020-0157-8>, 2020.

1068 Zhao, J. W., Wang, F., Zhan, R. F., Guo, Y. P., Huang, X., and Liu, C.: How Does Tropical Cyclone
1069 Genesis Frequency Respond to a Changing Climate?, *Geophysical Research Letters*, 50,
1070 <https://doi.org/10.1029/2023gl102879>, 2023.

1071 Zhao, Y. D. and Sun, D.-Z.: ENSO asymmetry in CMIP6 models, *Journal of Climate*, 35, 5555–5572,
1072 <https://doi.org/10.1175/jcli-d-21-0835.1>, 2022.

1073 Zhou, L., Bao, Q., Liu, Y. M., Wu, G. X., Wang, W. C., Wang, X. C., He, B., Yu, H. Y., and Li, J. D.:
1074 Global energy and water balance: Characteristics from Finite-volume Atmospheric Model of the
1075 IAP/LASG (FAMIL 1), *Journal of Advances in Modeling Earth Systems*, 7, 1–20,
1076 <https://doi.org/10.1002/2014MS000349>, 2015.

1077 Zi, P., Liu, Y. M., Li, J. D., Yang, R. W., He, B., and Bao, Q.: Reduced Spring Precipitation Bias and
1078 Associated Physical Causes over South China in FGOALS-f3 Climate Models: Experiments with
1079 the Horizontal Resolutions, *Journal of Meteorological Research*, 38, 784–804,
1080 <https://doi.org/10.1007/s13351-024-3200-4>, 2024.

1081 Zuo, H., Balmaseda, M. A., Tietsche, S., Mogensen, K., and Mayer, M.: The ECMWF operational
1082 ensemble reanalysis–analysis system for ocean and sea ice: A description of the system and
1083 assessment, *Ocean Science*, 15, 779–808, <https://doi.org/10.5194/os-15-779-2019>, 2019.